Cavitation in Creeping Shear Flows

Peter A. Kottke, Scott S. Bair, and Ward O. Winer
George W. Woodruff School of Mechanical Engineering, Georgia Institute of Technology, Atlanta, GA 30332

DOI 10.1002/aic.10480
Published online May 23, 2005 in Wiley InterScience (www.interscience.wiley.com).

Liquid failure has been observed in low Reynolds number (Stokes) shear flows where reduction of the hydrodynamic pressure should not occur. Cavitation in Stokes flows has implications in lubrication, polymer processing, and rheological measurements. Such cavitation can be predicted by a principal normal stress cavitation criterion (PNSCC). We present results of a direct experimental test of the PNSCC. Imaging of the cavitation events suggests that the cavitation is gaseous and originates from preexisting nuclei. Crevice-stabilized gas nuclei are assumed, and numerical simulations are used to investigate the cavitation event for a Newtonian liquid. The inception of cavitation from a preexisting nucleus, the persistence of suitable nuclei, and the growth and deformation of shed bubbles are considered. © 2005 American Institute of Chemical Engineers *AIChE J,* 51: 2150–2170, 2005

Introduction

Among the first reports of apparent liquid failure arising from an applied shear stress is that of Bair and Winer.[1] They demonstrated that variations of ambient pressure too small to affect viscosity had a pronounced effect on viscosity measurements in a Couette viscometer in which the magnitude of the shear stress τ_{xy} was near that of the pressure p. As a result, they proposed that cavitation occurs in a liquid when a principal normal stress becomes tensile. They later suggested the possibility that a lubricant could withstand a slight tension without cavitating.[2] Joseph independently proposed a similar criterion, introducing the possibility that the tensile strength σ_c could be positive or negative.[3] If $\sigma_c > 0$ then the liquid has some ability to withstand a tensile principal stress; if $\sigma_c = 0$ then the criterion is that originally proposed by Winer and Bair; and if $\sigma_c < 0$ then the liquid cavitates at some stress that is still compressive. The case of $\sigma_c < 0$ is analogous to the idea of a liquid cavitating if the hydrodynamic pressure is reduced to the vapor pressure. A principal normal stress cavitation criterion (PNSCC) with $\sigma_c = 0$ predicts shear cavitation, that is, cavitation in simple shear with no reduction of the hydrodynamic pressure, when the shear stress and the pressure are of the same order of magnitude.

Once the possibility of cavitation stemming from a shear stress of the order of the imposed hydrostatic pressure (usually 0.1 MPa) is considered, numerous examples of phenomena that may be explained by shear cavitation can be found. Archer et al.[4] found evidence of cavity formation at shear stresses in the range of 0.1 to 0.3 MPa for experiments performed at atmospheric pressure in low molecular weight polystyrene and α-D-glucose. Cogswell[5] found that high density polyethylene flow curves generated using a capillary tube viscometer show a decrease in the apparent viscosity of an order of magnitude at a shear stress of 0.2 MPa. He found a similar discontinuity in measurements obtained using a Couette viscometer at a shear stress of the order of 0.1 MPa. In both cases it seems that shear cavitation may be explanatory. Vinogradov[6,7] found that effects such as those reported by Cogswell are seen in many linear polymers; there is a critical stress in the range of 0.1 to 0.3 MPa for capillary tube viscometers, above which there is an abrupt decrease in apparent viscosity. Additionally, for the same liquids in rotational devices, an abrupt drop in torque and separation of the sample from the measuring surface occurs at a critical stress about half that seen in the capillary tube viscometer.[4,7] Son and Migler[8] published micrographs of cavities forming in polyethylene near the exit of a sapphire capillary where the shear stress is of the order of one atmosphere.

Polymer manufacturers use high-temperature, low-pressure processes combined with an application of a shear stress in devolatilization.[9] Favelukis et al.[10] found that, for a low molecular weight polybutene, vacuum was insufficient to cause

Correspondence concerning this article should be addressed to P. A. Kottke at peter.kottke@me.gatech.edu.

boiling and growth of gaseous bubbles. In addition, a critical level of shear was required. Their findings therefore suggest that polymer devolatilization processes sometimes rely on shear cavitation. In fact, the work of Favelukis et al. is part of a body of work in the area of shear effects on devolatilization and foaming, which has evolved a theory of shear-assisted nucleation that shares several aspects with the theory of shear cavitation that we present later in this work. In particular, Lee and Biesenberger[11] and Lee[12] postulated a metastable cavity model and concluded that within certain devolatilization regimes, bubble growth is determined by the transformation of shear energy into surface energy, and also by diffusive transport of the volatile species to the bubble. Chen et al.[13] and Guo and Peng[14] further developed the theory of mechanical shear energy conversion to surface energy in foaming processes, neglecting any role of diffusion. As will become apparent, a major difference between our model and those mentioned above is that we model the entire process as a free-surface problem with coupled transport of mass and momentum, rather than as a modification of classical nucleation theory.

There are several implications of the PNSCC. Some of the more obvious are in rheological measurements, where the assumption of a viscometric flow becomes invalid if cavitation has occurred. Of perhaps greater engineering significance are those real-world situations to which the rheological data would be applied. Cavitation could occur in polymer processing and lubrication applications where it has not been previously considered. In fact, Pereira et al.[15] demonstrated the effect of a PNSCC on cavitation in a journal bearing with axial throughput. A better understanding of the cavitation inception criterion will improve efforts at inhibiting cavitation when it is not desired, or ensuring cavitation when it is desirable.

In this work, we present experimental evidence supporting the suitability of the PNSCC for predicting cavitation in Newtonian liquids. We also combine our experimental observations with numerical and theoretical analyses to develop a consistent model of cavitation inception in shear. Our results suggest that the cavitation is gaseous, that it requires wall-stabilized nuclei with a positive interfacial curvature, and that subsequent bubble growth is through hydrodynamic deformation and accompanied by slow dissolution for the case of a gas-saturated liquid.

Principal normal stress cavitation criterion

The state of stress in a liquid is described by the stress tensor **T**. For an incompressible liquid this tensor can be split into two parts, a pressure component **p** and a deviatoric $\boldsymbol{\tau}$, where the deviatoric is the component that leads to deformation and flow of the liquid.

A tensile stress exists in the liquid whenever one or more of the principal stresses becomes positive. The principal stresses σ_1, σ_2, and σ_3 are the eigenvalues of **T**, and satisfy

$$\det(\mathbf{T} - \sigma\mathbf{I}) = 0 \tag{1}$$

where **I** is the identity tensor.

In simple shear, the deformation of a liquid can be expressed by a scalar, $\dot{\gamma}$, called the shear rate, and the deviatoric components of the stress tensor are functions of $\dot{\gamma}$ only. The simplest case is that of a Newtonian liquid in which the shear stress and shear rate are related by the Newtonian viscosity μ,

$$\tau_{xy} = \mu\dot{\gamma} \tag{2}$$

and the normal stress components of the deviatoric are zero.[16] In simple shear of a Newtonian liquid, the subscripts on the shear stress can be dropped. Thus, in the case of simple shear of a Newtonian liquid, the principal stresses are

$$\sigma_1 = -p + \tau \qquad \sigma_2 = -p \qquad \sigma_3 = -p - \tau \tag{3}$$

where σ_1 is the most tensile of the principal stresses. σ_1 is tensile for

$$\mu\dot{\gamma} > p \tag{4}$$

In the case of a generalized Newtonian shear thinning liquid the shear stress and shear rate are related by the non-Newtonian, or generalized, viscosity, $\eta(\dot{\gamma})$,

$$\tau = \eta(\dot{\gamma})\dot{\gamma} \tag{5}$$

and the analysis remains the same as for a Newtonian liquid with μ replaced by $\eta(\dot{\gamma})$.

The situation becomes more complicated in the case of liquids in which simple shear results in normal stress differences,

$$N_1 = \tau_{xx} - \tau_{yy} \qquad N_2 = \tau_{yy} - \tau_{zz} \tag{6}$$

We will consider the PNSCC in the context of Couette flow. For non-Newtonian liquids, we assume negligible N_2, and take the pressure at the edge of the flow to be p. In this case, the application of Eq. 1 to find the principal normal stresses yields

$$\begin{aligned}
\sigma_1 &= -p + \frac{1}{2}\left(N_1 + \sqrt{N_1^2 + 4\tau_{xy}^2}\right) \\
\sigma_2 &= -p + \frac{1}{2}\left(N_1 - \sqrt{N_1^2 + 4\tau_{xy}^2}\right) \\
\sigma_3 &= -p
\end{aligned} \tag{7}$$

The most tensile principal stress σ_1 is tensile for

$$\frac{1}{2}\left(N_1 + \sqrt{N_1^2 + 4\tau_{xy}^2}\right) > p \tag{8}$$

Cavitation and the tensile strength of liquids

Cavitation is defined as "the formation and activity of bubbles (or cavities) in a liquid."[17] The cavity may be created by the cavitation event, or be preexisting in the liquid in some manner, and caused to grow to macroscopic size by the cavitation event. The contents of the cavity may be vapor, gas, or a mixture of the two. Cavitation can be caused by local deposition of energy in a liquid or by tension in the liquid. In general, when discussing cavitation, the tension has been considered a result of pressure variations.

Liquids can withstand large uniform tensions, which can be considered negative absolute pressures.[18] Although most work concerned with the tensile strength of liquids has focused on water, lubricants and polymeric liquids have also been shown to be capable of reaching metastable states of negative pressure.[19] Based on the knowledge that a liquid can withstand tension, it might be expected that σ_c would be a large, positive number. Much work in cavitation has attempted to explain why cavitation occurs at pressures above that suggested by the theoretical tensile strength of a liquid. The most accepted theory was introduced by Harvey et al.[20] and expanded on by Apfel[21] and Crum.[22] They postulate that cavitation occurs in most cases through the growth of preexisting voids. These voids, called nucleation sites, are filled with gas. Surface tension increases the pressure inside a gaseous bubble in a liquid and, the smaller the radius of the bubble, the greater its internal pressure. The higher the pressure in the bubble, the greater the concentration difference driving diffusion of the gas out of the bubble. Therefore, a small gas bubble in a liquid requires some mechanism of stabilization to prevent its spontaneous disappearance. Several theories have been advanced for the method of nucleation site stabilization.

One widely accepted theory for nuclei stabilization is stabilization in a crevice on a solid impurity or bounding surface.[25-27] A crevice-stabilized gas nucleus can have an interface that is concave toward the liquid. Because of surface tension, the pressure of the gas in the nucleus can therefore be less than the pressure in the liquid and, if gas diffuses from the nucleus, so long as the contact line is pinned, the concavity will increase, reducing the pressure of gas. Thus such a nucleus can persist without completely dissolving into the liquid. The origin of such nuclei has been explained by considering the flow of a liquid onto a hydrophobic surface with crevices.[26] Another explanation of the origin and persistence of nuclei is that ordering of liquid molecules adjacent to solid surfaces leads to local hydrophobicity in regions of concavity of an otherwise nonhydrophobic surface.[27] This explanation suggests that the resulting voids have interfaces that are convex toward the liquids, and that their persistence is explained by a resonant behavior forced by ambient vibrations.

Although agreement on a theory of nucleation site stabilization has not been reached, it is generally accepted that stabilized gas bubbles are present in liquids and can act as nucleation sites.

Experimental

Apparatus

A Couette viscometer was constructed that allows visualization of the liquid sample undergoing shear and that allows for control of ambient pressure in a range of 15 to 300 kPa (Figure 1).

The viscometer is of the inner rotating-cylinder type. The outer cylinder is a commercially produced Pyrex® tube with an inner diameter of 1.593 cm. The inner cylinder, or bob, was produced by machining precipitation hardened steel, lapping the bob to the desired final diameter, and then polishing. The bottom of the inner cylinder is tapered to allow trapped gas bubbles to escape more easily. The outer diameter of the steel

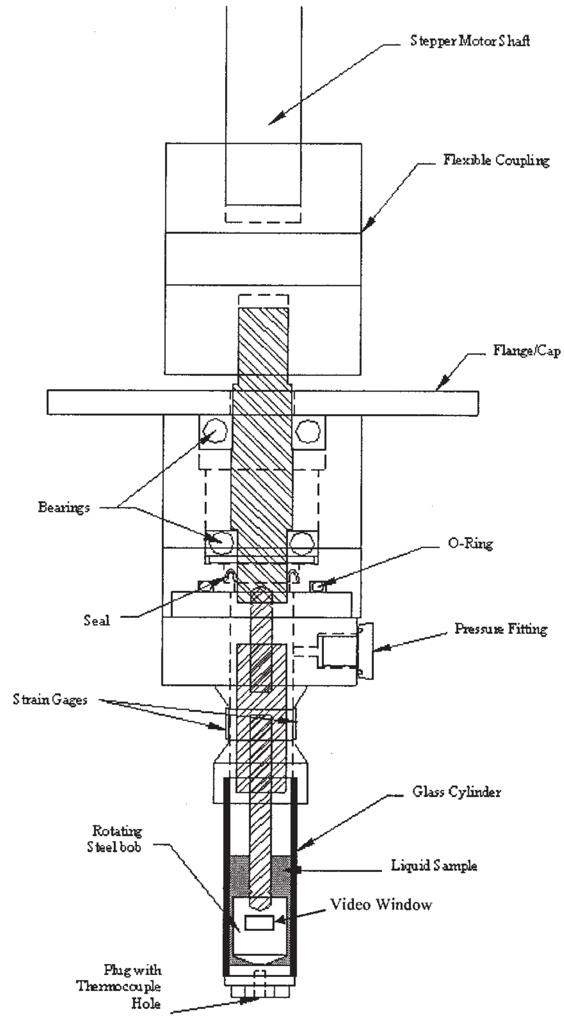

Figure 1. Variable-pressure Couette viscometer with flow cell.

bob was measured with a micrometer to be 1.582 cm and, upon calibration with a viscosity standard, the gap between the bob and Pyrex® cylinder was found to be 50 μm.

A DC stepper motor drives the bob, allowing the rate of shaft rotation to be specified. The stepper motor is connected to the drive shaft by a flexible coupling. The penetration of the pressure boundary by the shaft is sealed with a spring-energized Teflon® seal. An adjustable length shaft couples the drive shaft to the bob. The shaft connects to both the drive shaft and the bob with flexible joints, preventing the transmission of lateral thrust while permitting the transmission of torque. An O-ring–sealed pressure fitting also penetrates the pressure boundary, allowing connection of either a vacuum pump or pressurized gas source to the viscometer.

The determination of apparent shear stress in the liquid sample (τ_{app}) is accomplished by torque measurement using strain gauges attached to a thin-walled portion of the aluminum body of the viscometer. If the flow is viscometric, then the apparent shear stress is the shear stress at the glass surface. Because of the small ratios of gap to bob radius and gap to bob height, the apparent shear stress and shear stress in the gap will be nearly identical, provided the flow is parallel. The flow conditions in the experiments are such that there should be no instabilities; therefore, the apparent shear stress and the shear stress in the gap are essentially equal unless cavitation occurs.

Video/data-acquisition software was configured to allow simultaneous recording of the output from a digital camera and a digital signal. Output from the torque sensor was passed through a signal conditioner and A/D converter. The software was calibrated to record the signal as apparent shear stress, τ_{app}. The camera is monochrome with a maximum resolution of 1300×1030 pixels and with programmable exposure controls. It was fitted with a lens with a focal distance of 18 to 108 mm, which could provide $6 \times$ magnification.

Experimental liquids

The Couette viscometer was used to study shear cavitation in a polybutene (PB), H-1900, and a polydimethylsiloxane (PDMS), DC-200-10^6. Both liquids have limiting zero-shear viscosities of about 1000 Pa•s at room temperature. The PB is Newtonian to high shear stresses resulting from its low molecular weight, whereas the PDMS is expected to show non-Newtonian behavior at shear stresses of the order of 2×10^4 Pa. The PB is relatively temperature sensitive ($\beta = 0.027 \text{ K}^{-1}$), whereas the PDMS is not ($\beta = 0.007 \text{ K}^{-1}$); β is the temperature coefficient of viscosity.

Results

The effects of shear stresses up to and beyond the magnitude of the applied pressure were investigated for the PB and PDMS in the Couette viscometer. Experiments were performed at absolute pressures from 18 to 300 kPa, for apparent shear stresses from 10 to 270 kPa with shear rates up to 745 s^{-1}. The experiments were performed at liquid temperatures from 19 to 26°C.

The primary goal of the experiments was to determine at what level of shear stress, if any, cavitation occurs for various ambient pressures. The onset of cavitation was detected through visual observation; the recordings of apparent shear stress and video images of the sheared liquid are reviewed for indications of cavitation. Figure 2 shows images for different shear stresses in PB. Cavitation is clearly visible in the bottom two images. The widths (distance from top to bottom edge) of the voids in the images are between 0.01 and 0.1 cm.

The hypothesis being tested was one of zero critical stress, $\sigma_c = 0$. For PB this corresponds to cavitation occurring when the measured shear stress magnitude reaches the ambient pressure magnitude. For PDMS, nonzero normal stress differences were expected to result in cavitation at shear stresses of magnitudes less than the magnitude of ambient pressure.

Figure 3 shows the lowest shear stress at which cavitation was observed for PB and PDMS at pressures from 18 to 300 kPa. The hypothesized $\sigma_c = 0$ criterion predicts cavitation for τ above and to the left of the solid lines.

For PB, the liquid is Newtonian in the range of applied shear stresses, and the criterion takes the form of Eq. 4. PDMS on the other hand is non-Newtonian. The correct cavitation criterion is Eq. 8, which takes into account normal stress differences. To plot this criterion, in the absence of measured first normal stress difference coefficients (Ψ_1), a model must be incorporated to calculate the first normal stress differences. Wagner's model[28]

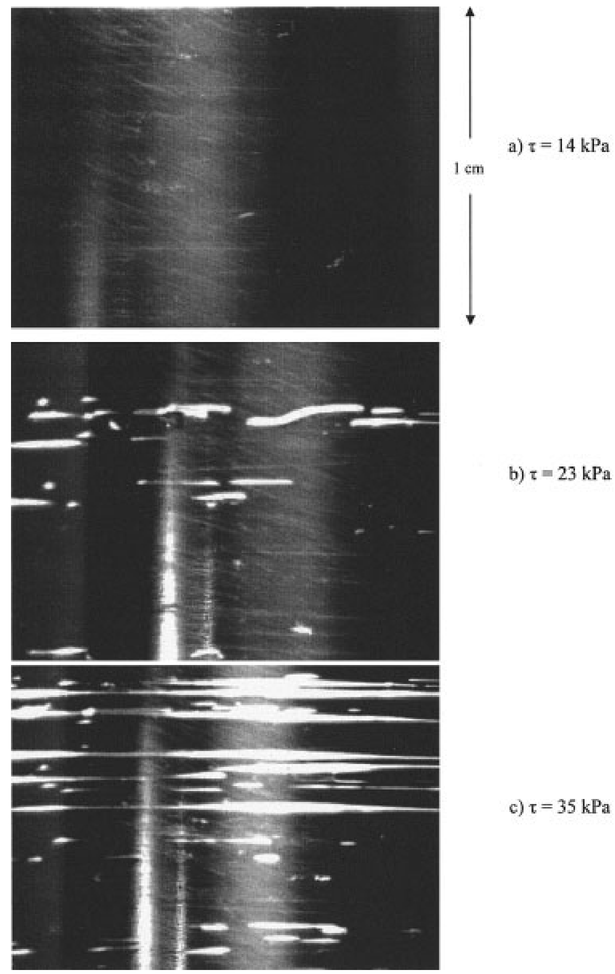

Figure 2. Polybutene (H-1900) 20°C, p = 19 kPa, sheared in 50-μm gap.

Cavitation is visible when shear stress was greater than the hydrostatic pressure.

$$\Psi_1(\dot{\gamma}) = -\frac{1}{z}\frac{d\eta}{d\dot{\gamma}} \tag{9}$$

was combined with a fit of shear-dependent viscosity to the Carreau–Yasuda equation[29] and measurements of first normal stress difference coefficients for PDMS,[30] to obtain a model for first normal stress difference coefficient Ψ_1

$$\Psi_1 = \Psi_{10}[1 + (\dot{\gamma}\lambda)]^{n-2} \tag{10}$$

The relaxation time λ was estimated using a result from molecular theory[16]

$$\lambda = \frac{\mu M}{\rho R_u T} \tag{11}$$

where M is the molecular weight and R_u is the universal gas constant; λ has a value of 0.07 s. The power-law index n comes from the shear-dependent viscosity data and is 0.3, whereas the low shear first normal stress difference coefficient Ψ_{10} is from

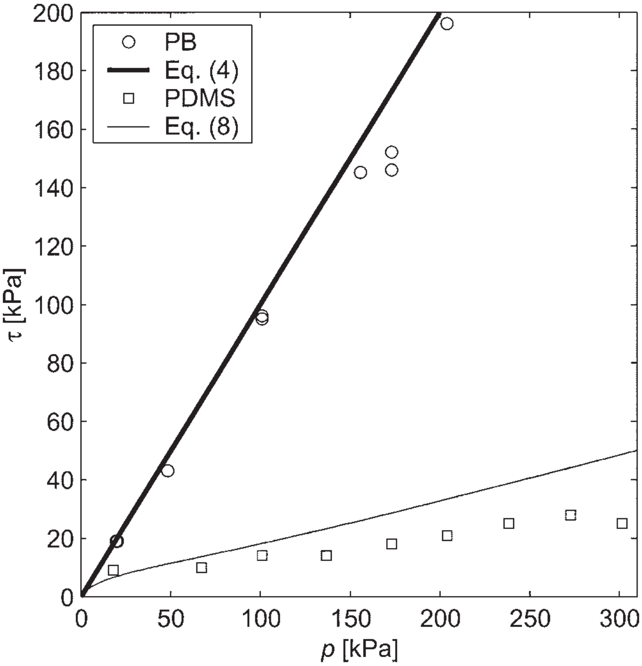

Figure 3. Shear stress of first observation of cavitation as a function of pressure for polybutene and polydimethylsiloxane.

The PNSCC with $\sigma_c = 0$ predicts cavitation for combinations of τ and p above and to the left of the solid lines.

a power-law fit of Gleiβle's data to molecular weight for PDMS,[31] and is 280 Pa·s^2. The resulting predictions of $N_1(\dot{\gamma}) = \Psi_1(\dot{\gamma})\dot{\gamma}^2$ were qualitatively verified by comparison with extrudate swell observations.[31]

For the Newtonian liquid, PB, the results demonstrate good agreement with the hypothesis; however, for PDMS, the predicted shear stress is higher than the observed shear stress at cavitation. The error increases as the shear stress exceeds the modulus $G = \mu/\lambda = 14$ kPa, a strong indicator that the deviation is the result of non-Newtonian behavior.

From experiment we have seen that for a Newtonian liquid (PB) in simple shear, cavities grow visible when the shear stress equals the ambient pressure. This is predicted by a principal normal stress cavitation criterion with a critical stress of zero. However, we can also show experimentally that liquids can withstand tension when the liquid is first pressurized to eliminate preexisting voids.[19] Therefore, a critical stress of zero suggests that the cavitation originates from preexisting voids. Stabilization of voids in a liquid can be explained by void formation in a crevice on some solid surface.[25] A reasonable hypothesis is that shear cavitation occurs when the shear flow causes the growth of such preexisting voids to macroscopic size. The observation that multiple voids are frequently observed in the same horizontal band provides further support to the concept of inception from wall-crevice–stabilized nuclei. Based on the perseverance of voids after the removal of the shear stress, especially at reduced pressures, it is likely that the cavitation process is primarily one of gaseous cavitation. Thus the void fills with gas that was in solution in the liquid, rather than vapor.

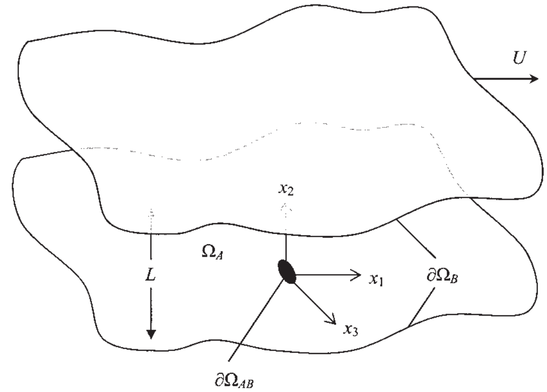

Figure 4. Liquid domain (Ω_A) for the general model for inception of shear cavitation.

Theory and Simulation: Inception

A general model for cavitation from a crevice-stabilized gas nucleus consists of two systems: (1) the liquid with dissolved gas, Ω_A; and the void, or gas bubble, Ω_B (Figures 4 and 5). The two systems interact at the interface surface $\partial\Omega_{AB}$. The liquid system Ω_A is semi-infinite; it is bounded by parallel solid walls, $\partial\Omega_A$, above and below (x_2^* equals L and 0, respectively), and unbounded in the x_1^* and x_3^* directions. The upper portion of $\partial\Omega_A$, at $x_2^* = L$, is translating in the x_1^* direction at a constant speed U. Note that throughout the remainder of this work asterisks (*) denote the dimensional form of the variable.

The gas system Ω_B is finite. Ω_B is bounded above by the gas–liquid interface $\partial\Omega_{AB}$, and below by the solid, unmoving crevice. The intersection of the gas–liquid interface $\partial\Omega_{AB}$ with the lower solid surface $\partial\Omega_A$ is the contact line $\partial^2\Omega_{AB}$. The coupled systems are governed by laws of momentum conservation, energy conservation, and species conservation. We pursue a greatly simplified model.

The natural length, velocity, and timescales are L, U, and L/U. Based on the cavitation criterion, the pressure scaling is chosen to be a viscous scale: $\mu U/L$. We assume that Henry's law, $c^* = Hp_G^*$, governs the concentration of dissolved gas c^*, at a gas–liquid interface, with gas pressure p_G^*. Based on a dissolved gas concentration in Ω_A far from the void resulting from an interface between the liquid and gas at pressure p_∞^*, the scale for dissolved gas concentration in the liquid is $c_s = Hp_\infty^*$.

In Ω_A the liquid is assumed to be Newtonian and the flow is incompressible. The model is isothermal and the properties are

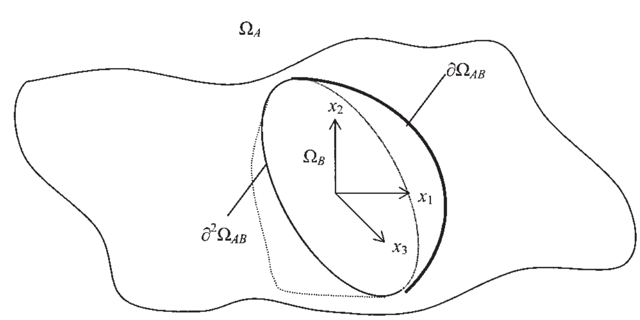

Figure 5. Gas domain (Ω_B) for the general model for inception of shear cavitation.

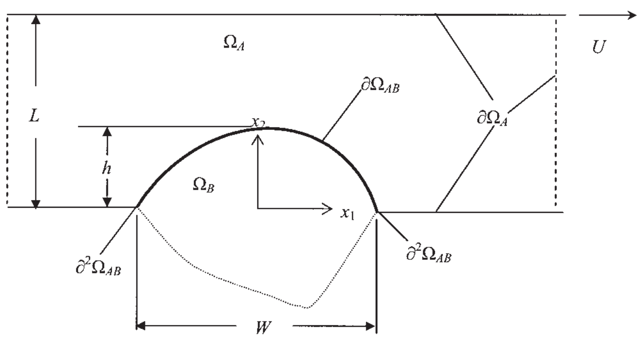

Figure 6. Two-dimensional model for inception of shear cavitation.

assumed to be uniform. Therefore the flow in Ω_A is governed by the scaled Navier–Stokes equations. Body forces are neglected. Assuming Fickian diffusion and a constant binary mass diffusivity of gas in the liquid D, the mass transport of dissolved gas in the liquid is governed by the transient advection–diffusion equation.

In the Couette experiments using polybutene

$$L \sim 10^{-5}\ \text{m} \qquad \mu \sim 10^3\ \text{Pa}\cdot\text{s} \qquad \rho \sim 10^3\ \text{kg m}^{-3}$$
$$U \sim 10^{-3}\ \text{m s}^{-1} \qquad D \sim 10^{-10}\ \text{m}^2\ \text{s}^{-1} \quad (12)$$

These values give a Reynolds' number, $\text{Re}_L = \rho UL/\mu$, of order 10^{-8}, and Peclet number, $\text{Pe}_L = UL/D$, of order 10^2 for PB.

In the Couette experiments using polydimethylsiloxane

$$L \sim 10^{-5}\ \text{m} \qquad \mu \sim 10^2\ \text{Pa}\cdot\text{s} \qquad \rho \sim 10^3\ \text{kg m}^{-3}$$
$$U \sim 10^{-2}\ \text{m s}^{-1} \qquad D \sim 10^{-9}\ \text{m}^2\ \text{s}^{-1} \quad (13)$$

(The low shear viscosity for PDMS is 10^3 Pa·s, but, the experiments show cavitation at a shear stress for which shear thinning has reduced the viscosity by about an order of magnitude.) The values in Eq. 13 give a Reynolds' number, $\text{Re}_L \sim 10^{-6}$, and Peclet number, $\text{Pe}_L \sim 10^2$ for PDMS.

Based on the very small Reynolds numbers, consideration is limited to the Stokes approximation, in which inertial effects are neglected and the equations governing the flow in Ω_A are quasi-steady.

In the experiments, L is 50 μm, whereas the voids generally have a width of about 500 μm. This observation suggests that a two-dimensional model for bubble growth may be appropriate. Indeed, previous investigations of bubble and droplet deformations have found that two-dimensional models yield pertinent and valuable information to the three-dimensional case.[32] Therefore a two-dimensional model will be used as a simplified cavitation model (Figure 6).

The gas in the void Ω_B is assumed to be isothermal and to obey the scaled ideal gas equation of state

$$p_B = CiHR_u T c_B \tag{14}$$

where the convention of using the subscript B to indicate in the bubble has been introduced. Ci is the cavitation index, defined as $Ci = p_\infty^*(\mu U/L)^{-1}$. Ci is unity when the shear stress equals the far-field pressure. A principal normal stress cavitation criterion with a critical stress of zero predicts cavitation for $Ci < 1$.

Conservation of mass for the void requires

$$\frac{dN_B}{dt} = -(\text{Pe}_L)^{-1} \int_{\partial\Omega_{AB}} \frac{\partial c}{\partial n}\, ds \tag{15}$$

where N_B is the number of moles of gas per unit depth in Ω_B, scaled by $Hp_\infty L^2$, and the spatial derivative in the integrand is with respect to the direction of the normal vector pointing into the void.

On the solid surfaces $\partial\Omega_A$, the no-slip, no-penetration condition is applied, and, far from the void, the presence of the void no longer perturbs the flow. The gas in Ω_B is treated as inviscid; therefore, on the gas–liquid interface, f_t, the tangential component of the traction vector, is zero. The interface is assumed to have an isotropic surface tension, γ, and thus on $\partial\Omega_{AB}$, f_n, the normal component of the traction vector in the liquid, is the sum of the bubble pressure and the Laplace pressure ($\kappa\gamma$, where κ is the curvature of the interface). The traction is scaled with a viscous scale to be consistent with the pressure scale and the curvature is scaled with the inverse of the length scale.

The kinematic condition on the gas–liquid interface, $\partial\Omega_A$, requires the position of the interface, $\mathbf{x}_{\partial\Omega_{AB}}$, to be advected with the local velocity $\mathbf{u}$

$$\frac{d\mathbf{x}_{\partial\Omega_{AB}}}{dt} = \mathbf{u} \qquad \text{on } \partial\Omega_{AB} \tag{16}$$

There are two limiting cases for which the solution of the advection–diffusion equation for mass transfer becomes unnecessary. One is the case of an impermeable liquid ($\text{Pe}_L \rightarrow \infty$), for which there is no mass transport from the liquid to the void and thus N_B remains constant. The other is the case of infinitely fast diffusion ($\text{Pe}_L \rightarrow 0$), for which the concentration of gas in the void c_B remains constant. These cases, analogous to the heat-transfer models of adiabatic and isothermal systems for fast and slow processes, respectively, provide two different vantages from which to consider the model for cavitation, and they substantially simplify the solution. They are reasonable approximations whenever the timescale for bubble growth attributed to deformation is much faster (impermeable liquid) or slower (infinite diffusion) than the timescale for bubble growth resulting from diffusion of gas in or out of the bubble.

To obtain some information about the role of mass transfer for conditions such as those in the experiments, a third model is incorporated. This model, accurate only if the system has a sufficiently high Peclet number, is the "penetration model," in which the mass transfer is calculated based on the assumption that a quasi-steady concentration boundary layer surrounds the bubble.[33] For such a case, in dimensional variables

$$\frac{dN_B^*}{dt^*} = FD\,\frac{c_\infty^* - Hp_B^*}{\delta_c}\,S_B^* \tag{17}$$

with

$$\delta_c = S_B^* \mathrm{Pe}_{S_B^*}^{-1/2} \tag{18}$$

where S_B^* is typically the bubble circumference, δ_c is the scale of the concentration boundary layer thickness, $\mathrm{Pe}_{S_B^*}$ is the Peclet number based on S_B^* and the maximum tangential velocity on the bubble surface $u^*_{\max}$, and F is an order one factor that depends on the flow geometry. When scaled, Eq. 17 becomes

$$\frac{dN_B}{dt} \approx \left(c_\infty - \frac{p_B}{Ci}\right)\mathrm{Pe}_L^{-1/2}(u_{\max}S_B)^{1/2} \tag{19}$$

Although F generally changes with the flow geometry, it will remain order one; we have set F to unity for calculations. Models such as Eq. 19 are typically applied when the flow over the bubble is unidirectional[33] or symmetric.[10] The situation in our simulations is more complicated because areas of recirculation can form near the trailing edge of the bubble, thus making the boundary layer model clearly inappropriate. Therefore, the length S_B is defined as the arclength along the bubble surface from the rear contact line to the point where the tangential component of the surface velocity is zero.

A contact line exists at the interface of three different phases: in the case of this work a solid, liquid, and gas phase. In the two-dimensional model, reference to the contact line is actually a reference to one of two points. De Gennes[34] reviewed contact line dynamics and provides a common nomenclature. The contact angle θ is defined as the angle measured in the liquid at the contact line between the solid–liquid boundary ($\partial\Omega_A$) and the gas–liquid boundary ($\partial\Omega_{AB}$). The contact line is said to be advancing when the motion would cause the area of contact between the liquid and solid to increase and receding when the motion would cause the area of contact between the liquid and solid to decrease. The contact line velocity $\mathbf{u}_{\mathrm{CL}}$ is defined in a reference frame so that it assumes a positive value when the contact line is advancing and a negative value when the contact line is receding. The contact angle for a stationary contact line, $\mathbf{u}_{\mathrm{CL}} = 0$, can be theoretically predicted using thermodynamic arguments[34]

$$\cos\theta_s = \frac{\gamma_{GS} - \gamma_{LS}}{\gamma_{LG}} \tag{20}$$

where the subscript s indicates static, and the subscripts on the surface tensions indicate the phases separated by the relevant interface: gas (G), solid (S), or liquid (L).

The contact angle should deviate from the theoretical value expressed in Eq. 20 only when the system is not in equilibrium. However, chemical heterogeneities and surface roughness allow the contact angle to achieve apparent equilibrium at a range of values, leading to the phenomenon of contact angle hysteresis or contact line pinning. In such cases, the contact line advances when the contact angle exceeds a certain value, the advancing contact angle θ_A, and recedes when the contact angle falls below the receding contact angle θ_R.

In the two-dimensional model there are two contact lines: the point at the interface of the gas, liquid, and solid boundary located initially at positive x_1 is called the front or leading contact line, and the other is called the rear contact line. When the contact line is located at a point where the solid surface experiences a discontinuity in slope there are two possible contact angles. Which is relevant depends on whether the contact angle will be compared with the advancing or receding contact angle. For a contact line located at either corner between the wall and crevice, the contact angle that should be compared with the advancing contact angle is the angle between the gas–liquid interface and the crevice wall at the contact line, whereas the contact angle that should be compared with the receding contact angle is the angle between the gas–liquid interface and the horizontal wall surface.

The no-slip assumption results in a nonintegrable (and nonphysical) singularity at the contact line attributed to a discontinuous velocity.[35] Proper resolution of the contact line singularity and the development of a contact line model for incorporation into a hydrodynamic model is a continuing subject of research. When the bulk flow is of primary interest, and details of the flow very near the contact line are not important, a successful, although ad hoc, approach is to assume that some relationship exists between the apparent dynamic contact angle and the contact line velocity.[36] Many such relationships have been proposed, based on experimental data or analyses.[37-39] In the absence of experimental data specific to the geometry, materials, and flow of interest, the choice of model is somewhat arbitrary. The model developed by Hoffman[37] was later recast in an explicit form that has been successfully used by other researchers and forms the basis of our contact line model[40]

$$\frac{\cos\theta - \cos\theta_s}{\cos\theta_s + 1} = \tanh(4.96\mathrm{Ca}_{\mathrm{CL}}^{0.702}) \tag{21}$$

where the contact line capillary number $\mathrm{Ca}_{\mathrm{CL}}$ is based on the contact line velocity

$$\mathrm{Ca}_{\mathrm{CL}} = \frac{\mu|\mathbf{u}_{\mathrm{CL}}|}{\gamma} \tag{22}$$

Replacing the static contact angle with the appropriate choice of advancing or receding contact angle, and rewriting Eq. 21 for $\mathrm{Ca}_{\mathrm{CL}}$ as an explicit function of the contact angle, yields the model used for this work

$$\mathrm{Ca}_{\mathrm{CL}} = \left\{\begin{array}{ll} -0.1018\left[\tanh^{-1}\left(\dfrac{\cos\theta_R - \cos\theta}{1-\cos\theta_R}\right)\right]^{1.425} & \theta < \theta_R \\ 0 & \theta_R \le \theta \le \theta_A \\ 0.1018\left[\tanh^{-1}\left(\dfrac{\cos\theta - \cos\theta_A}{\cos\theta_A + 1}\right)\right]^{1.425} & \theta > \theta_A \end{array}\right\} = \mathcal{H}^{-1}(\theta;\theta_A,\theta_R) \tag{23}$$

The mathematical model that is solved in an attempt to gain insight into cavitation inception from crevice-stabilized gas nuclei in a simple shear flow is a two-dimensional model in which a liquid system and gas system are coupled. The liquid system is governed by the Stokes equations for fluid flow and the gas system obeys the ideal gas equation of state. The limits of infinitely fast diffusion and an impermeable liquid are considered. Alternatively, a quasi-steady boundary layer model is used to approximate mass transfer. The simplified two-dimensional model is quasi-static

$$\nabla^2\mathbf{u} = \nabla p \qquad \nabla\cdot\mathbf{u} = 0 \tag{24}$$

$$u_2 = 0 \qquad \text{at } x_2 = 0 \qquad u_1 = 1 \qquad \text{at } x_2 = 1 \tag{25}$$

$$\left.\begin{array}{r} u_2 \rightarrow 0 \\ f_n \rightarrow -Ci \end{array}\right\} \qquad \text{as } x_1 \rightarrow \pm\infty \tag{26}$$

$$u_{\mathrm{CL}} = \mathrm{Ca_L}\mathscr{H}^{-1}(\theta;\, \theta_A,\, \theta_R) \qquad \text{at } \partial^2\Omega_{AB} \tag{27}$$

$$f_t = 0 \qquad \text{on } \partial\Omega_{AB} \tag{28}$$

$$f_n = \frac{\kappa}{\mathrm{Ca}_L} + p_B \qquad \text{on } \partial\Omega_{AB} \tag{29}$$

$$p_0 = p_B(t = 0) = Ci + \frac{\kappa_0}{\mathrm{Ca}_L} \tag{30}$$

$$p_B = p_0 \tag{31}$$

or

$$p_B = \frac{A_B(t = 0)}{A_B(t)}\, p_0 \tag{32}$$

or

$$p_B = \frac{N_B(t)}{A_B(t)}\frac{A_B(t = 0)}{N_B(t = 0)}\, p_0 \tag{33}$$

The initial bubble pressure p_0 is set in Eq. 30 based on the initial curvature κ_0 so that the system is in mechanical equilibrium in the absence of flow.

The equation for p_B is Eq. 31 in the case of infinitely fast diffusion. For an impermeable liquid, the bubble pressure depends only on the variation of the bubble area A_B, with time, and so Eq. 32 applies, whereas Eq. 33 is used along with Eq. 19 for the penetration model. Ca_L is the capillary number: $\mathrm{Ca}_L = \mu U/\gamma$. It is a measure of the strength of the viscous stress relative to surface tension. For simulations, the crevice geometry is simplified to that of a triangle or trapezoid and specified using a crevice area, A_C, which is the area between the crevice walls and a horizontal line drawn across the crevice mouth, and crevice angles θ_{CL} and θ_{CR}, which are the angles between the left or right walls of the crevice and vertical.

Equations 24 to 33 are an ideal system of equations for solution by the boundary element method (BEM), which is based on an integral formulation of the governing equations and has been applied to problems involving moving interfaces in Stokes flows with considerable success.[41] The BEM has a number of advantages, the greatest of which is that, for a linear, quasi-steady problem such as ours, it reduces the dimensionality of the problem, eliminating the need to discretize the interior of domain Ω_A. Our implementation of the BEM draws heavily on the published experience of researchers who have used it for similar problems. Pozrikidis[42,43] used the BEM to study two-dimensional bubbles in infinite shear flows. First Dimitrakopoulos and Higdon[44] and later Schleizer and Bonnecaze[45] used the BEM to look at the displacement of two-dimensional incompressible droplets from walls in shear flows.

The general solution method involves recasting the governing equation in terms of a boundary integral equation with both known and unknown values of the traction and velocity in the integrals, multiplied by kernel functions

$$u_j(\mathbf{x}_0) = -\frac{1}{2\pi}\int_{\partial\Omega_A,\partial\Omega_{AB}} f_i(\mathbf{x})G_{ij}(\mathbf{x},\mathbf{x}_0)dl(\mathbf{x}) + \frac{1}{2\pi}\int_{\partial\Omega_A,\partial\Omega_{AB}} u_i(\mathbf{x})T_{ijk}(\mathbf{x},\mathbf{x}_0)n_k(\mathbf{x})dl(\mathbf{x}) \tag{34}$$

where n_k is the inward pointing normal, and

$$G_{ij} = -\delta_{ij}\ln(r) + \frac{\hat{x}_i\hat{x}_j}{r^2} \qquad T_{ijk} = -4\frac{\hat{x}_i\hat{x}_j\hat{x}_k}{r^4}$$
$$\hat{x}_i = x_i - x_{0i} \qquad r = \sqrt{\hat{x}_1^2 + \hat{x}_2^2} \tag{35}$$

The boundary is discretized and the unknown velocities and tractions are approximated as constants on each element. The boundary integral equation thus becomes a linear system of equations that is solved for the unknown velocities and tractions. The velocities on the interface are used to advance the interface position in time, using an adaptive second-order Runge–Kutta time integration method.[46] For the impermeable liquid and penetration model the pressure in the bubble is updated as the interface position changes. The velocities at the contact lines during the time stepping are determined from the contact angles and Eq. 27, and thus do not appear explicitly in the integral formulation.

With the boundary conditions for the crevice-stabilized gas nuclei problem (Eqs. 25–29) the boundary integral equation (Eq. 34) is a Fredholm integral equation of mixed kind, and there is no theory that allows the determination of uniqueness or existence of solution.[47] Uniqueness of solution is an important question because the related integral formulation of the problem of a free, compressible, inviscid bubble in a shear flow, if solved using Eq. 34, does not have a unique solution.[42] In other words, although the solution to the formulation of the Stokes flow problem as a system of differential equations (that is, Eq. 24), has a unique solution, this does not guarantee uniqueness for the integral formulation. Practically speaking, nonuniqueness results in an ill-conditioned matrix when the integral equation is discretized, and the condition number will become larger as the number of elements is increased. This suggests a nonrigorous method to check the uniqueness of solution by monitoring matrix condition number. For the problem of the deformation of an inviscid bubble attached to a wall, the matrices do not have the ill-conditioned nature indicative of a nonunique solution. However, nonuniqueness of solution precludes the use of our BEM simulation program to investigate the fate of any bubbles shed from the nucleation site;

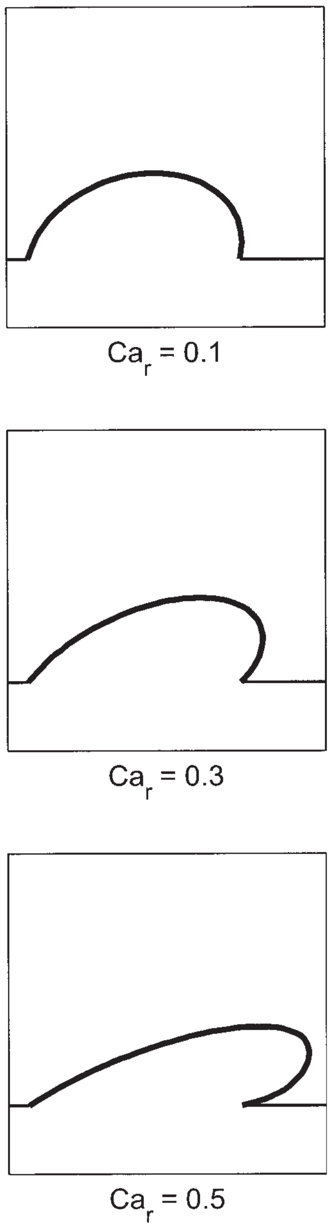

Figure 7. Steady-state shapes for initially semicircular bubbles.

With $Ci = 1000$ the bubble area stays nearly constant; thus the shapes can be compared with the results of Feng and Basaran.[48] $Ca_r = Ca(W/2)$ is the capillary number based on the initial bubble radius.

although it may be possible to eliminate this problem through modifications of the integral equation,[42,47] we chose a different approach, discussed in the section on bubble deformation and growth, to study the fate of shed bubbles.

Inception simulation results

We compare the results of simulations allowed to progress to steady-state conditions to those of Feng and Basaran,[48] who used a finite-element method to find steady solutions for bubbles with a specified final cross-sectional area. Our interface shapes are shown in Figure 7 for comparison with their Figure 5, and the close agreement is used to validate our computer code.

To determine whether a two-dimensional model of inception from wall-stabilized nuclei agrees with the experimental results, simulations are performed in the range of Ca_L corresponding to experimental conditions ($Ca_L \sim 30–290$ for PB), and for Ci near unity. Because no gas nuclei could be observed in the experiments before shearing, the dimensionless crevice width W is limited to a maximum of 0.2.

Simulations with zero initial curvature for an interface with contact lines on the crevice corners show that the interface is stable to shear for any Ca_L, Ci, and W; the normal component of the velocity is zero everywhere on the interface. Because the interface does not deform, the mass-transfer model does not matter in this case, provided the liquid is saturated; the interface does not deform if $\kappa_0 = 0$.

If the liquid is undersaturated, simulations incorporating mass transfer have an initially negative curvature. If the liquid is supersaturated, simulations incorporating mass transfer have an initially positive curvature. Impermeable liquid cases can have any initial curvature. Figure 8 shows interface positions for various times for two simulations, one of infinite diffusion with $\kappa_0 < 0$ (undersaturated) and one for a case of no diffusion with $\kappa_0 < 0$. The main result in Figure 8 is general for all

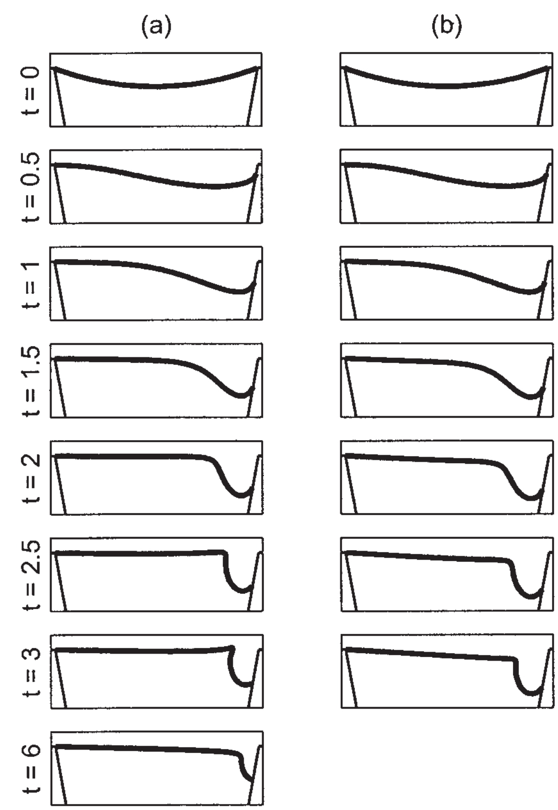

Figure 8. Simulations of interface deformation from initially negative curvature for infinitely fast diffusion (a) and impermeable liquid (b).

For both (a) and (b) $\kappa_0 = -5$, $Ca_L = 150$, $Ci = 1$, $W = 0.1$, $\theta_{CL} = \pi/12$, $\theta_{CR} = \pi/12$, $A_C = 1.87 \times 10^{-3}$, $\theta_A = 2\pi/3$, and $\theta_R = \pi/2$. No combination of these parameters was found for which an initially negatively curved interface escaped the crevice.

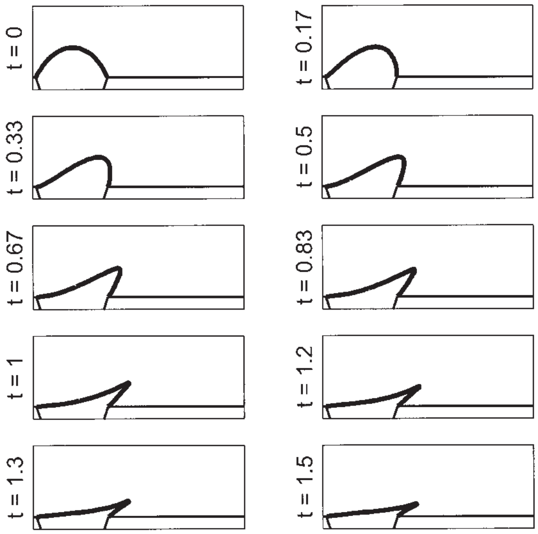

Figure 9. Simulation results for initially positive curvature and infinitely fast diffusion.

Interface positions at intervals of $t = 1/6$ for a simulation with $Ca_L = 100$, $Ci = 1$, $W = 0.1$ and $\kappa_0 = 16$. The contact lines are pinned.

permutations of the other parameters investigated with $\kappa_0 < 0$; a bubble with an initially negatively curved interface will not escape the crevice. This is a very important result. The crevice model for nuclei stabilization typically uses the fact that a crevice can cause a bubble to attain a negative curvature to explain nuclei persistence. If all crevice-stabilized gas nuclei interfaces have a negative curvature, then the most obvious conclusion must be that either the cavitation observed in the experiments does not originate from wall-crevice–stabilized nuclei or the two-dimensional model cannot capture the relevant physics. There is, however, another reasonable conclusion, which is that the experimentally observed cavitation together with the results in Figure 8 suggests that gas nuclei in wall crevices can persist for long periods of time with a positive interface curvature. This agrees with the nucleation site stabilization model proposed by Mørch.[27] We present an alternate explanation in the following section for the persistence of nuclei with positive curvature. For the remainder of this work we assume that such nuclei are present.

Figure 9 shows interface positions for various times for the case of infinite diffusion with $\kappa_0 > 0$ (supersaturated), and Figure 10 shows interface positions for an impermeable liquid with $\kappa_0 > 0$. Both simulation results exhibit some common characteristics. Initially, the bubbles are compressed and the bubble area decreases. This is similar to the behavior exhibited by a free two-dimensional bubble in an infinite shear flow.[42] For the case of infinitely fast diffusion, the pressure does not increase during this period of compression; therefore, there is less resistance to compression and the reduction in area is greater and occurs for a longer time. Also, the following expansion is much less vigorous for the diffusion case. Finally, the shape of the bubble at later times shows a cusp or near cusp. Such cusps may have a role in production of tip-streaming bubbles,[49,50] but tip streaming under these conditions is not a well-understood phenomenon. As will be seen shortly, the impermeable liquid model, for the same conditions, predicts bubble shedding stemming from pinch-off. Diffusion can therefore play one of two roles in the shedding of bubbles from nucleation sites in shear: either it inhibits it or it shifts the mechanism from pinch-off to tip streaming.

Examination of the interface shapes for the impermeable liquid case (Figure 10) shows that by $t = 4.3$ the bubble has deformed considerably and two opposing sides have come into contact at a "pinch-off" point. It can be assumed that by this time a portion of the bubble downstream of the pinch-off point will have detached, becoming a free bubble. Absent mass transfer, the portion of the bubble that remains will achieve a steady-state shape. Only one bubble will be shed. Even when the impermeable liquid model is appropriate for simulating the shedding of a bubble, diffusion may still be important in later bubble growth, given that the timescale for the subsequent bubble growth could be considerably longer than the timescale for the shedding process. The fate of shed bubbles is discussed in the section on bubble deformation and growth.

Figure 11 shows interface shapes for a case in which mass transport is simulated using the penetration model. For this simulation, the initial conditions and parameters not related to mass transport are the same as those for the simulations depicted in the previous two simulations (infinitely fast diffusion and impermeable liquid models, respectively). The parameter that describes the level of saturation of dissolved gas in the liquid, c_∞, is chosen for this simulation so that the initial curvature is stable

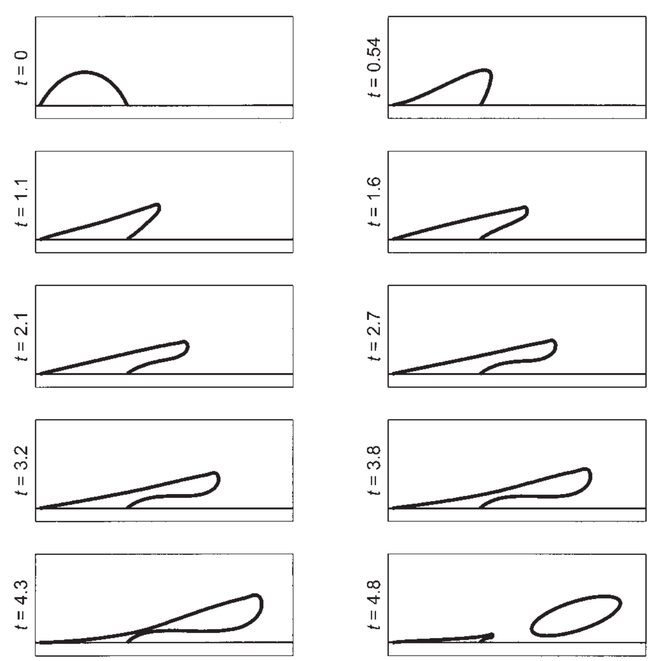

Figure 10. Simulation results for initially positive curvature and no diffusion.

Interface positions at successive times t for a simulation with $Ca_L = 100$, $Ci = 1$, $W = 0.1$ and $\kappa_0 = 16$ (no diffusion). The contact lines are pinned and the crevice cross sectional area A_C is zero. At $t = 4.3$ the interface touches itself and the bubble is assumed to "pinch off" at the point of contact. The shed portion of the bubble is not included in later times for the inception simulations using the BEM.

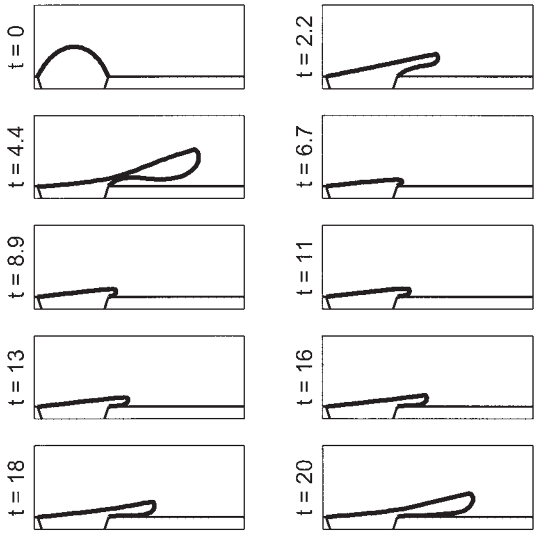

Figure 11. Simulation results for initially positive curvature using the penetration model.

Interface positions at successive times t for a simulation with $\mathrm{Ca}_L = 100$, $Ci = 1$, $W = 0.1$, $\kappa_0 = 16$, $c_\infty = 1.16$ and $\mathrm{Pe}_L = 1000$. The contact lines are pinned and the crevice cross sectional area A_c is zero. At $t = 4.6$ the interface touches itself and the bubble is assumed to "pinch off" at the point of contact. The shed portion of the bubble is not included in later times for the inception simulations using the BEM. The simulation demonstrates how a nucleation site could shed multiple bubbles when the liquid is gas supersaturated.

$$c_\infty = 1 + \frac{\kappa_0}{Ci\mathrm{Ca}_L} \tag{36}$$

The Peclet number Pe_L is related to the capillary number Ca_L

$$\mathrm{Pe}_L = \mathrm{Ca}_L \frac{L\gamma}{\mu D} \tag{37}$$

For the simulation in Figure 11 the Pe_L is 1000, which is at the high end of its range for the experiments with the Couette viscometer.

For the early times shown in Figure 11 the deformation of the interface is substantially similar to that in Figure 10. Pinch-off occurs slightly later and the shed bubble is a little smaller, in keeping with the inhibiting effect of diffusion on pinch-off. Whereas for the impermeable liquid model case depicted in Figure 10 only a single shedding event occurs, and for the infinitely fast diffusion case in Figure 9 no bubble is shed, Figure 11 shows that for boundary layer type mass transfer in a supersaturated gas–liquid solution, multiple bubbles may be shed. Mass transfer generally increases the level of shear necessary for shedding to occur, although it is necessary for continual shedding.

For an impermeable liquid, whether a nucleation site bubble will deform to the point that it will pinch-off depends on crevice cross-sectional area A_C, as well as Ci, Ca_L, and h, and also on the advancing and receding contact angles, crevice shape, and the relative nearness of the far wall W. When $Ci = 1$, and choices of the other parameters that are consistent with the experiments, pinch-off will occur when $\mathrm{Ca}_L h$ exceeds 0.64. This value is not universal; it depends on crevice geometry, advancing and receding contact angle values, and the relative nearness of the far wall. In general, a lower crevice cross-sectional area promotes pinch-off (lowers the necessary value of $\mathrm{Ca}_L h$): the value given above, 0.64, is for $A_C = 0$. Pinch-off requires higher $\mathrm{Ca}_L h$ when the liquid is more hydrophobic, as well as for higher W. Contrary to expectations, as Ci increases, so does the critical value of $\mathrm{Ca}_L h$, as demonstrated in Figure 12.

Changing the applied pressure, as was done in the experiments, has several possible effects. If the pressure change is extreme then the properties of the liquid could change. If the pressurization is done with gas, then the concentration of dissolved gas in the liquid changes. The cavitation index Ci changes for the same applied shear stress, which has effects already discussed. Finally, nuclei will respond mechanically to pressure changes; this mechanical response can include motion of the contact line into or out of the crevice.[26]

The mechanical response of wall-stabilized nuclei to pressure changes, neglecting contact line motion, sheds considerable light on the linkage between the simulations and experimental results. Increases in pressure result in a reduction of h, and if h for a given site is driven below zero then the site will be deactivated, that is, it will not shed a bubble regardless of whether the shear stress is applied. Similarly, sites that would not have shed bubbles can be activated through pressure reduction. The mechanical response of a nucleation site depends on the initial bubble volume, the crevice geometry, and the contact line dynamics, θ_A and θ_R. In general, the smaller the bubble volume, the less it will respond to pressure increases. Recalling that smaller crevice volumes promote pinch-off, it seems likely that the cavitation events observed experimentally originated from shallow crevices. The experimental results with PB are replotted as h vs. p by assuming that the observed

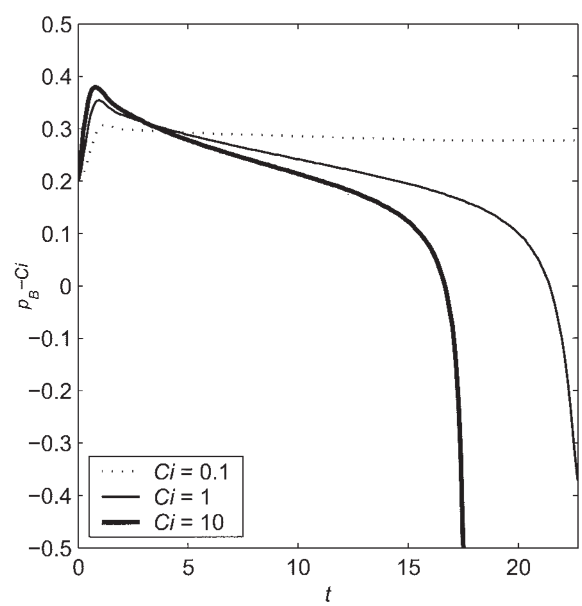

Figure 12. Effect of *Ci* on pinch-off.

Variation of bubble pressure above Ci showing effect of Ci on pinch-off for baseline conditions (except for Ci) and $\mathrm{Ca}_L = 50$, $\kappa_0 = 10$ ($\mathrm{Ca}_L h = 0.67$). The thick line is the result of a simulation with $Ci = 10$, the thin line for $Ci = 1$, and the dotted line for $Ci = 0.1$. As Ci decreases, pinch-off is inhibited.

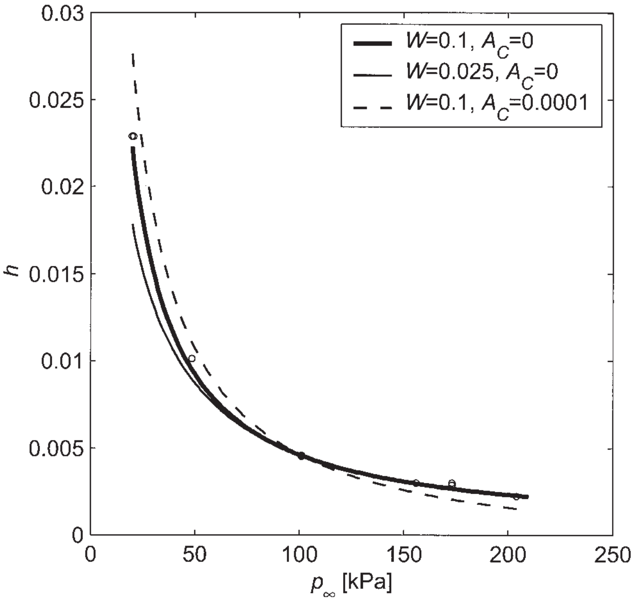

Figure 13. Link between PNSCC and simulation results.

Mechanical response of critical void to pressure changes (lines) plotted against the height that a given void would need to have based on experimental inception of cavitation, assuming inception occurs when $\mathrm{Ca}_L h = 0.64$.

inception of cavitation occurred at $\mathrm{Ca}_L h = 0.64$ (Figure 13). Using the data points at $p = 100$ kPa to set a reference $h(p = 100 \text{ kPa}) = h_0$, curves can be generated for a given A_C and W, showing the mechanical response of a bubble to pressure changes. The curves in Figure 12 are for $W = 0.1$ and $W = 0.025$ in the limit of crevice cross-sectional area $A_C = 0$, and for $W = 0.1$ with $A_C = 10^{-4}$. The PB data, which supported a PNSCC with critical stress σ_c of zero, lie close to the curve for $W = 0.1$, $A_C = 0$.

Theory and Simulation: Persistence of Nuclei

One of the more important conclusions drawn from the simulation of cavitation inception from wall-attached gas nuclei is that the cavitation nuclei have positive curvature (that is, are convex toward the liquid). This is counter to the typically held view of such nuclei, which would permit a positive curvature only if the liquid were supersaturated with dissolved gas. Otherwise, the reasoning goes, the positive curvature would result in a Laplace pressure that would keep the bubble pressure above the liquid pressure. Thus diffusion would drive gas from the bubble until it had zero curvature, if the bulk liquid were saturated, or negative curvature if the bulk liquid were undersaturated. There are other theories that predict persistent nuclei with positive curvature. Mørch[27] proposed that ambient vibrations lead to resonance in voids in local wall concavities, resulting in rectified diffusion and stable nuclei with positive curvature. Crum[22] presented hypotheses of stabilization ascribed to an ionic or surface-active skin on bubbles in water. We have performed an analysis that relaxes the need for such explanations by greatly extending the time a nucleus would be expected to persist with positive curvature.

The details of the analysis are provided in the Appendix. The analysis starts with a model for dissolution of a spherical bubble of initial radius $R^* = R_0$ in a viscous liquid, neglecting inertial effects, and approximating the concentration gradient at the bubble surface. In dimensionless form the model is

$$\dot{R} \approx \frac{p_B - p_\infty}{4} R - \frac{1}{2}$$

$$\dot{p}_B \approx -3\Pi_1 \frac{(p_B - p_\infty)}{R}\left(\frac{1}{R} + \frac{\Pi_2 t^{-1/2}}{\sqrt{\pi}}\right) - 3p_B \frac{\dot{R}}{R}$$

$$\Pi_1 = \frac{R_u THD\mu}{\gamma R_0} \qquad \Pi_2 = \sqrt{\frac{R_0\gamma}{D\mu}} \tag{38}$$

and has initial conditions

$$R(0) = 1 \qquad p_B(0) = p_\infty + 2 \tag{39}$$

which are chosen so that the bubble is initially in mechanical equilibrium. The model depends on three parameters: p_∞, Π_1, and Π_2.

The system consists of a pair of coupled nonlinear ordinary differential equations (ODEs) that can easily be numerically integrated, provided the singularity at $t = 0$ is avoided by starting at some slightly positive time. In essence, this is initially assigning some large but finite concentration gradient, instead of the artificial infinite gradient required by the initial conditions of the model. The model is verified by plotting against the results of simple experiment in which bubble dissolution in PDMS was videotaped and the images were used to obtain a plot of bubble radius vs. time (Figure 14). After an initial period in which the variation of bubble radius is affected by concentration gradients resulting from the diffusion from surrounding bubbles, the model and data show very good agreement. Data on diffusivity and solubility of air in polybutene could not be found. To obtain estimates of these properties, the same bubble radius experiment was performed on PB and then an optimization routine was used to find the values of H and D that give the best fit to the data. These are the property values given in Table 1 for PB. Figure 14 shows plots of the data against the model for PDMS and PB. The model can be used to determine whether viscous effects are important for a given bubble size. For PDMS, viscous effects are important, although not dominant, for bubbles where $R_0 < 10$ μm, whereas for PB viscous effects are not noticeable unless $R_0 <$ 1 μm. When viscous effects are important, they always extend the bubble dissolution time.

The analysis is modified next for a bubble on a conical crevice, and then, because viscous effects are found to have only a negligible effect on bubble dissolution time, they are neglected to develop a model for dissolution of a cylindrical bubble. This cylindrical bubble model is used in the development of a model for dissolution of a bubble in a long surface scratch, which is a single ODE for the dimensionless curvature κ:

$$\dot{\kappa} = -\frac{8}{\pi^2}\Pi_1 \frac{\sin^{-1}(\kappa)}{R_{eq}(\psi + A_B + A_C)} \int_0^\infty \frac{\exp\left(-\dfrac{t}{\Pi_2^2 R_{eq}^2}\tau^2\right)}{\tau[J_0^2(\tau) + Y_0^2(\tau)]} d\tau \tag{40}$$

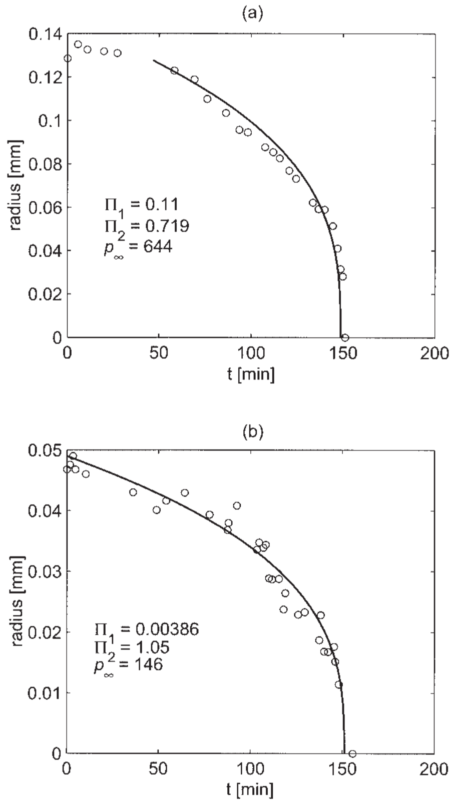

Figure 14. Bubbles in PDMS (a) and PB (b) were videotaped during dissolution.

Plots of bubble radii vs. time for PDMS are plotted to validate the model of bubble dissolution (Eq. 38), whereas for PB the data are used to obtain estimates of the transport properties H and D.

where

$$\psi = \frac{2\kappa(p_\infty + \kappa)[1 - \cos(2\sin^{-1}\kappa)] + (2p_\infty + \kappa)[\sin(2\sin^{-1}\kappa) - 2\sin^{-1}\kappa\sqrt{1-\kappa^2}]}{2\kappa^3\sqrt{1-\kappa^2}} \tag{41}$$

and

$$R_{eq} = \frac{\int_{-\sin^{-1}(\kappa)}^{\sin^{-1}(\kappa)} \sqrt{2 - \kappa^2 - 2\cos(\theta)\sqrt{1-\kappa^2}}\,d\theta}{2\kappa\sin^{-1}(\kappa)} \tag{42}$$

Finally, the effect of an opposing parallel wall (distance $d = L/R_0$ away) on the diffusion from a crevice-stabilized cylindrical bubble is considered by using Eq. 40 until

Table 1. Liquid Properties at 20°C

	γ (N m^{-1})	μ (Pa · s)	D (m^2 s^{-1})	H (mol m^{-3} Pa^{-1})
PDMS	0.020	1000	1.57×10^{-9}	7.34×10^{-5}
PB	0.034	1000	0.48×10^{-9}	0.55×10^{-5}

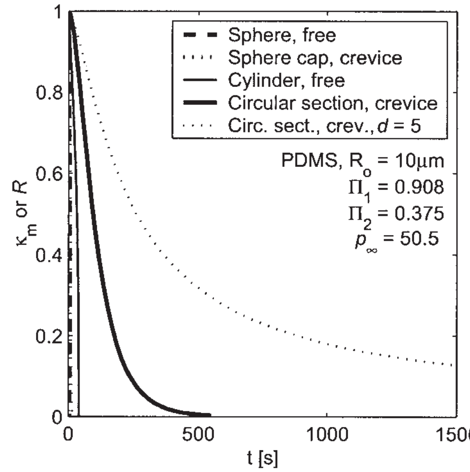

Figure 15. Plot comparing bubble dissolution in PDMS.

$$t > 10\,\frac{\Pi_2^2(d\kappa - 1 + \sqrt{1-\kappa^2})^2}{\pi\kappa^2} \tag{43}$$

after which the following is used

$$\dot{\kappa} = -\frac{8}{\pi^2}\Pi_1\kappa\,\frac{1-\sqrt{1-\kappa^2}}{R_{eq}(\psi + A_B + A_C)}\int_0^\infty \frac{\exp\left(-\frac{t}{\Pi_2^2 R_{eq}^2}\tau^2\right)}{\tau[J_0^2(\tau) + Y_0^2(\tau)]}\,d\tau \tag{44}$$

Figures 15 and 16 compare nondimensional R or κ for free or crevice-bound bubbles, respectively, as functions of dimensional time for the four categories of bubbles in PDMS and PB, with dimensional $R_0 = 10$ μm and $p_\infty = 100$ kPa. The crevice volume and area are calculated assuming a cone or triangle with base angle of $\pi/2$. For the case of a bounded domain, $d = 5$. The liquid properties used in the figures are in Table 1. The surface tension and dynamic viscosities were provided by the manufacturer, with viscosities verified in this lab. The diffusivity and Henry's constant, H, for PDMS were found using

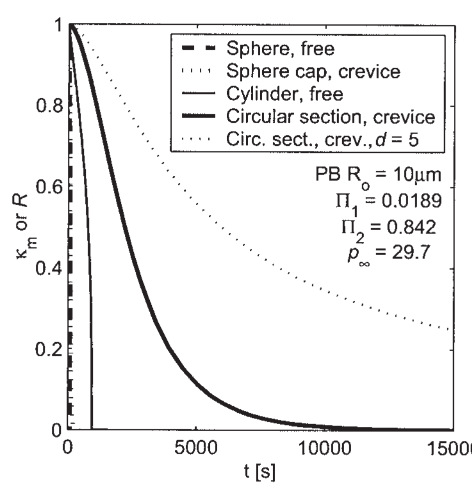

Figure 16. Plot comparing bubble dissolution in PB.

published data and an Arrhenius-type correlation for temperature correction.[51]

The conclusion drawn from the analyses is that wall-crevice–stabilized gas nuclei with positive curvature can persist for long periods of time, provided they form in scratchlike crevices. Confinement of the liquid to a gap whose thickness is not too much greater than the crevice width greatly retards the rate of curvature decrease.

Theory and Simulation: Deformation and Growth of Bubbles

Once a bubble has detached from a nucleation site, its fate can be considered the result of the linked processes of migration, deformation, and advection/diffusion controlled growth or dissolution. Bubble shedding is necessary but not sufficient for cavitation inception; it must be followed by subsequent growth.

The lateral motion of a droplet or bubble resulting from a shear flow and in the presence of a wall has been studied analytically,[52] numerically,[53] and experimentally,[54] with the general result being that deformable droplets move laterally away from a wall in shear flow. A recent work looks at higher-order solutions and finds a range of viscosity ratios for which the direction of migration can change[55]; however, the inviscid bubble is well outside this range. As droplet deformation increases (that is, at higher capillary number) the rate of lateral migration increases. Also, most of the studies report that the rate of migration decreases as the square of separation distance between the wall and droplet increases. Therefore, it is to be expected that shed bubbles will move away from the wall toward the center of the shear flow.

An approximate model for bubble growth accurate for bubbles that have migrated far from the wall and whose cross-stream dimensions are small compared to L is a bubble in an infinite shear flow. Crowdy[56] developed a model for the transient deformation of a compressible bubble in infinite shear with an arbitrary time-dependent bubble pressure. The model is an extension of the work of Richardson,[57] who transformed the steady-state problem into a boundary value problem in analytic function theory, and the work of Tanveer and Vasconcelos,[32] who developed a class of exact solutions applicable to bubble pressures of zero. Although the variation of bubble pressure in Crowdy's model is ostensibly for investigation of effects of the gas equation of state, it is an ideal formulation for linking the fluid mechanics model to a mass-transfer model, by varying the bubble pressure arising from changes in both area and mass. Crowdy's model yields a time-dependent conformal mapping from the unit circle in the complex plane to the free bubble surface. The mapping is found by numerically solving a pair of coupled ODEs, Eqs. 3.9 and 3.10 in Crowdy's paper.

We modify Crowdy's model by including a model for mass transfer. Mass transfer is incorporated with the penetration model (Eq. 19), where S_B is half the bubble circumference, and the rate of change of N_B is multiplied by a factor of 2 to account for the presence of two, symmetric concentration boundary layers. A scaling analysis of bubble growth and dissolution in shear performed by Favelukis et al.[58] looked at the same model, in essence, in the asymptotic limits of $\mathrm{Ca}_L \to 0$ and $\mathrm{Ca}_L \to \infty$ for three-dimensional bubbles. Note that the requirement of a high Peclet number for applicability of the penetration model is not met for all shed bubbles in our simulations, the relevant definition of Peclet number being $u^*_{\max} S^*_B/D$. Using Crowdy's model without any mass transfer, Peclet numbers fall into the range of 1–1000, with higher Peclet numbers occurring later in time and for higher capillary number. Nevertheless, we limit our consideration to the penetration model for mass transfer. Note also that, although we retain our earlier scaling for consistency of notation, the distance L is not a relevant parameter for an infinite shear flow, and all quantities containing L are multiplied by R_0, the scaled initial (equivalent) radius, which satisfies

$$p_B(0)A_B(0) = [Ci + (\mathrm{Ca}_L R_0)^{-1}]\pi R_0^2 \tag{45}$$

where R_0 is the radius of a circular bubble with $N_B(0)$ moles of gas per unit depth and at mechanical equilibrium in a quiescent liquid with scaled far-field pressure Ci.

It is helpful to first consider the response of a bubble to shear in the absence of mass transfer.[42] Two-dimensional bubbles that are initially circular deform through a series of elliptical shapes. If a bubble is initially in mechanical equilibrium, then it will first be compressed and then it will expand; the final pressure is always less than the initial pressure. The reduction in pressure is greater for bubbles with higher $\mathrm{Ca}_L R_0$ and lower $Ci\mathrm{Ca}_L R_0$. We can use Crowdy's model without mass transfer (isothermal ideal gas equation of state, N_B constant) to consider the fate of shed bubbles in the impermeable liquid case. The simulation of bubble shedding in an impermeable liquid depicted in Figure 10 is used as a basis for the initial conditions for the demonstrative example depicted in Figure 17. The shed bubble increases by almost an order of magnitude in apparent length (Δx_1), which is the projection of S_B normal to the far-field flow direction; therefore the full event from bubble shedding through shed bubble deformation can be considered a cavitation inception event. The final bubble shape is sheetlike, which agrees with experimental observations.

It can be deduced that a bubble must dissolve if at steady state

$$p_B > c_\infty Ci \tag{46}$$

where $c_\infty = 1$ for a gas-saturated system, <1 for an undersaturated system, and >1 for a supersaturated system. It is found through solution of Crowdy's model that for two-dimensional bubbles, for all combinations of Ci, Ca_L, and R_0, $p_B > Ci$ at steady state. For instance, in the case depicted in Figure 17, $p_B \to 1.125Ci$. It seems that dissolution must eventually occur for shed bubbles unless the liquid is supersaturated with gas.

Typical rates of dissolution are found using the same initial conditions used for the simulation shown in Figure 17, but incorporating the penetration model. For these examples, shown in Figure 18, the liquid is assumed to be gas saturated, $c_\infty = 1$, and the transport properties of PB and PDMS (Table 1) with the experimental value $L = 50$ μm are the basis for choosing $HR_uT = 0.015$ and $\mathrm{Pe}_L = 400$ (PB) and $HR_uT = 0.2$ and $\mathrm{Pe}_L = 60$ (PDMS). The results using the transport properties of PB show that up to $t = 40$ there is little difference between the impermeable model and penetration model results; a reduction of the mass in the bubble by 20% occurs by $t = 90$. The greater diffusivity and higher Henry's constant of PDMS result in enhanced mass transfer. When using those transport properties, the bubble shrinks more rapidly. By $t = 9$ the bubble modeled using PDMS properties has reached a maximum apparent length, and by $t = 17$ it has lost sufficient mass that its pressure begins to increase. The pressure increase occurs as the capillary number based on equivalent radius, $\mathrm{Ca}_L R_0$, decreases, and the shear flow loses its ability to deform the bubble. The bubble returns to a more compact, circular shape, leading to higher bubble pressures and greater driving gradient for mass transfer. The mass transfer is higher than it would be in a quiescent liquid arising from advection effects, and once the pressure begins to increase, the bubble quickly disappears.

If the liquid is supersaturated, $c_\infty > 1$, then the shed bubble's mass may eventually increase. Recall that the bubble shedding example, based on the penetration model (Figure 11), used a supersaturated liquid, $c_\infty = 1.16$ and $\mathrm{Pe}_L = 1000$. An ellipse with the same area as the portion pinched off from the bubble, and at the pressure at the pinch-off time for the simulation used to generate Figure 11, was used for the initial conditions for a simulation of bubble deformation and growth in a supersaturated solution, $c_\infty = 1.16$. The results of the simulation, shown in Figure 19, are an example of bubble deformation leading to unstable growth. At $t = 16$, the bubble pressure = (far-field pressure) $\times$ (the degree of saturation c_∞), and the number of moles of gas per unit depth is at a global minimum. For all times $t > 16$ the mass flux will be into the bubble, increasing its capillary number based on equivalent radius, and thus lowering the pressure that the bubble would reach at steady state in the absence of mass transfer. This results in a positive feedback loop, where mass flux into the bubble increases the driving gradient for mass transfer. The apparent bubble length increases substantially. Physically, this cycle would be ended by depletion of the dissolved gas in solution in the liquid.

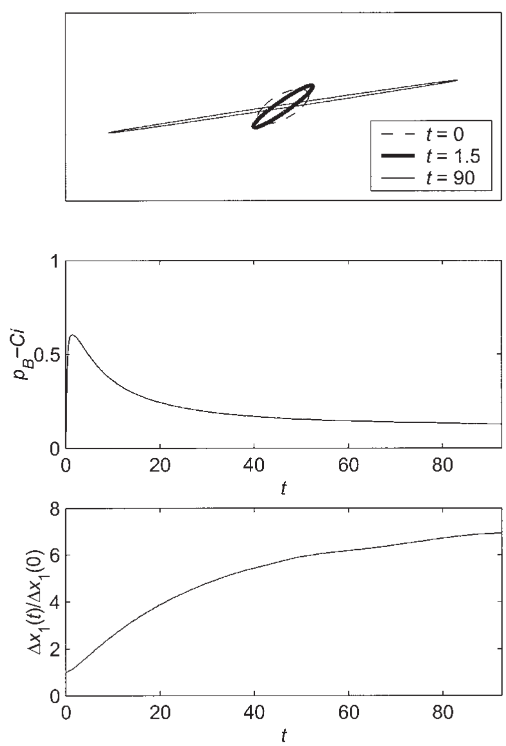

Figure 17. Bubble deformation in an impermeable liquid, $\mathrm{Ca}_L = 100$, $Ci = 1$.

The initial conditions are based on the simulation depicted in Figure 10. The initial pressure is the pressure in the void at pinch-off in that simulation ($t = 4.3$) and the initial shape is an ellipse with the same area as the area that was detached from the crevice-stabilized void (shown in the last frame of Figure 10). The top frame shows the bubble shape at three times t: the initial shape (dashed line), the shape at the time of maximum compression $t = 1.5$ (thick line), and the steady-state shape (thin line). The middle frame shows the variation of bubble pressure with time: $p_B - Ci$ approaches 0.125. The bottom frame shows the evolution of apparent bubble length to an observer looking down from the x_2 direction. The apparent bubble length increases by almost an order of magnitude, resulting from deformation.

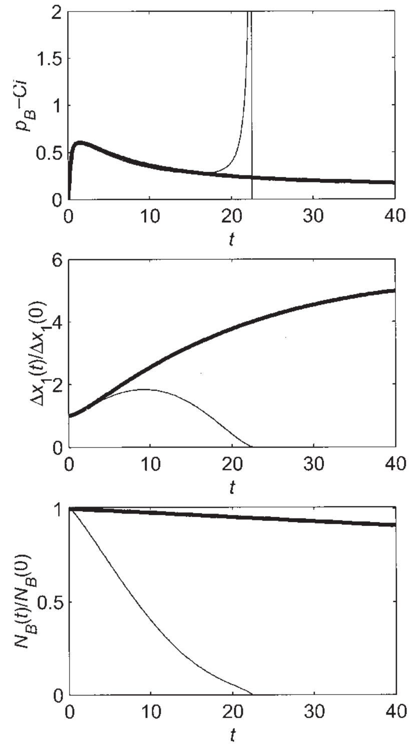

Figure 18. Bubble deformation using the penetration model, $\mathrm{Ca}_L = 100$, $Ci = 1$, $c_\infty = 1$.

The initial conditions are based on the simulation depicted in Figure 10. The initial pressure is the pressure in the void at pinch-off in that simulation ($t = 4.3$) and the initial shape is an ellipse with the same area as the area that was detached from the crevice-stabilized void (shown in the last frame of Figure 10). Two cases are shown, one using PB transport properties (thick lines) and the other using PDMS properties (thin lines). The top frame shows the variation of bubble pressure with time; the middle frame the evolution of apparent bubble length to an observer looking down from the x_2 direction; and the bottom frame the variation of the number of moles of gas per unit depth in the bubble with time. The simulation using PB properties is very close to the impermeable liquid model (Figure 17) for the time range shown, although it will eventually dissolve. The bubble simulated using PDMS properties dissolves rapidly.

Conclusions

In this work we have considered aspects of the role of tension in simple shear flows, which are frequently used to measure rheological properties. Our interest is in the possibility that such flows could lead to cavitation when the shear stress is sufficiently large (of the order of the pressure). There is very

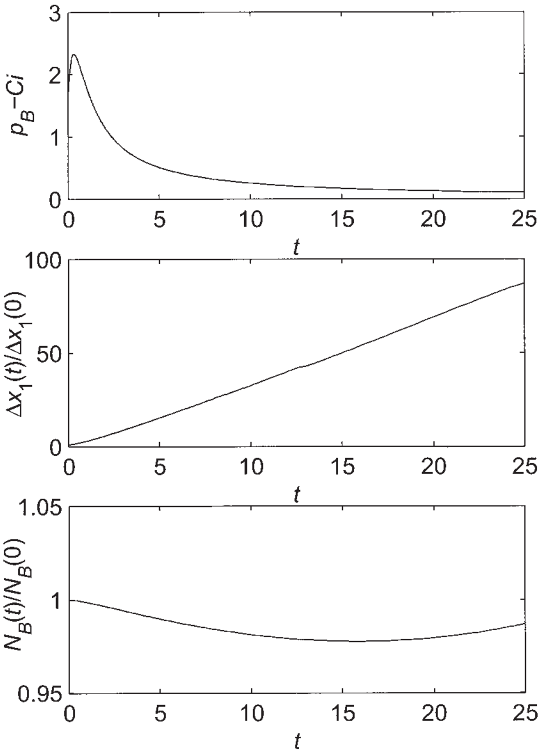

Figure 19. Deformation and growth of a shed bubble in a gas-supersaturated liquid.

Initial conditions are based on the inception simulation using the penetration model and leading to a shed bubble (Figure 11). The parameters for the simulation of bubble growth and deformation using the penetration model are $\mathrm{Pe}_L = 1000$, $HR_uT = 0.025$, $Ci = 1$, and $\mathrm{Ca}_L = 100$. After $t = 16$ the mass transfer is into the bubble, resulting in ever increasing apparent bubble length.

little prior research into this concept, although there has been considerable research into the related field of the influence of shear to nucleation under supersaturated conditions. We consider the problem from two different perspectives.

The first method of investigation is an experimental test of a principal normal stress cavitation criterion (PNSCC), which is attractive because of its simplicity, its appeal to physical intuition, and the large number of cases in the literature of some sort of apparent strong rheological change at shear stresses near atmospheric pressure in magnitude. Our experiment constitutes the first direct test of the PNSCC, and we find that the PNSCC accurately predicts cavitation in a Newtonian liquid (PB). However, its performance is a little less satisfactory for the non-Newtonian test liquid (PDMS). Finally, it is difficult to reconcile the idea of failure of a liquid in shear with no apparent tensile strength to the fact that liquids exhibit an ability to withstand large tensions in the absence of cavitation nucleation sites; and if the presence of such nucleation sites is assumed, then the PNSCC seems overly simplistic.

Consequently, the second method of investigation is an analysis, for the case of a Newtonian liquid, of cavitation inception in shear from wall-stabilized gas nuclei. We have presented a theoretically consistent picture, backed by simulation results, of cavitation inception from wall-stabilized nuclei. Three stages of inception were considered, with original contributions in each. These include an analysis of wall-stabilized nucleus dissolution, boundary element method simulations of crevice-stabilized, inviscid, compressible bubble deformation in a bounded shear flow with mass transfer, and an analysis of the deformation and dissolution or growth of an inviscid compressible bubble in infinite shear with mass transfer.

The simulations of shear deformation of wall-stabilized gas nuclei bring to light several important concepts tempered by a number of significant assumptions. The most important assumption is that the two-dimensional model can capture the relevant physics. The two most important results are that nuclei must have positive curvature (that is, be convex toward the liquid) for the deformation to lead to a shed bubble, and that within the realistic range of other parameters, deformation will lead to pinch-off when $\mathrm{Ca}_L h \sim 1$. Another result of the simulations is that, all other things being equal, a bubble on the cavity with the smallest cross-sectional area A_C is most likely to deform to pinch-off. Considering, therefore, the mechanical response of sites with small A_C to pressure changes, we find that in the range of pressures and crevice sizes considered, the height the bubble extends above the wall h is roughly inversely proportional to the applied pressure. Consequently, the criteria for pinch-off based on $\mathrm{Ca}_L h$ leads to a prediction that the shear stress needed for pinch-off is proportional to the pressure. If the proportionality constant is nearly unity then the PNSCC with $\sigma_c = 0$ is a good predictor of cavitation.

A final result of the bubble shedding simulations that is important to the overall picture is the role of mass transport. Three models were used: (1) an impermeable liquid model; (2) the quasi-steady boundary layer, or penetration, model; and (3) the infinitely fast diffusion model. The effect of mass transport is to raise the required level of shear for pinch-off to occur because mass transport will always mitigate the pressure increase during the initial compression of the bubble. If the liquid is supersaturated then mass transport can replenish a nucleation site after a bubble is shed. If the liquid is saturated then the simulations suggest that only a single shedding event will occur.

We demonstrate, through an approximate analysis, that nuclei that approach the two-dimensional limit maintain positive curvature ($\kappa > 0$) for long times, especially when an opposing wall hinders diffusion. This provides an explanation for the type of voids typically seen in the experiment, and provides some support for the use of a two-dimensional model for inception.

We also consider the fate of shed bubbles. The results clearly demonstrate that shed bubbles deform considerably, becoming long and slender (sheetlike). The results also suggest that absent gas supersaturation, all shed bubbles will eventually disappear.

Despite the experimental investigation of both a Newtonian and a non-Newtonian liquid, the simulation results consider Newtonian behavior only.

As a final caveat, although we consider the demonstration of feasibility and consistency of our model that treats all major stages of bubble nucleation, agreeing with experimental results to be a convincing argument that this is a good theory, we acknowledge that it is far from proof that this is the mechanism by which shear cavitation occurs, and other hypotheses could be argued as convincingly. Having gained insight into expected behavior of the critical shear stress for cavitation inception based on simulations, a return to experimental work to see whether the model predictions are correct is needed before alternate theories of cavitation in shear are abandoned. Similarly, more involved simulations could be used to validate some of the assumptions used in this work, in particular the two-dimensional model and the penetration model, although such simulations would be computationally expensive.

Frequently, when shear stresses are of the magnitudes considered here, they are occurring in liquids that exhibit strongly non-Newtonian behavior. Modeling shear cavitation inception for non-Newtonian liquids is a topic that would prove very interesting, though challenging.

Finally, satisfied that a clear picture of cavitation in shear is emerging, the understanding of this phenomenon should be applied to enhance or inhibit cavitation as desired. Liquid treatment (degassing or prepressurizing), surface coating, the use of surfactants, and surface etching and polishing could all be used to alter the cavitation behavior.

Acknowledgments

We thank Anthony Schleizer and Darren Crowdy for their helpful correspondences regarding implementation of the BEM for droplets attached to walls, and calculation of tangential velocities on free bubbles, respectively.

Literature Cited

1. Bair S, Winer WO. Influence of ambient pressure on the apparent shear thinning of liquid lubricants—An overlooked phenomenon. Conference Publication 1987-5. Vol. 1. London: Institute of Mechanical Engineers; 1987:395-398.
2. Bair S, Winer WO. The high pressure high shear stress rheology of liquid lubricant. *J Tribol*. 1992;114:1-9.
3. Joseph DD. Cavitation and the state of stress in a flowing liquid. *J Fluid Mech.* 1998;366:367-378.
4. Archer LA, Ternet D, Larson RG. "Fracture " phenomena in shearing flow of viscous liquids. *Rheol Acta.* 1997;36:579-584.
5. Cogswell FN. The influence of pressure on the viscosity of polymer melts. *Plast Polym.* 1973;14:39-43.
6. Vinogradov GV, Ivanova LI. Wall slippage and elastic turbulence of polymers in the rubbery state. *Rheol Acta.* 1967;7:243-254.
7. Vinogradov GV. Viscoelasticity and fracture phenomenon in uniaxial extension of high-molecular linear polymers. *Rheol Acta.* 1975;14: 942-954.
8. Son Y, Migler KB. Cavitation of polyethylene during extrusion processing instabilities. *J Polym Sci Part B: Polym Phys*. 2002;40:2791-2799.
9. Albalak RJ. *Polymer Devolatilization*. New York, NY: Marcel Dekker; 1996.
10. Favelukis M, Tadmor Z, Semiat R. Bubble growth in a viscous liquid in simple shear. *AIChE J.* 1999;45:691-695.
11. Lee ST, Biesenberger JA. A Fundamental study of polymer melt devolatilization. IV: Some theories and models for foam enhanced devolatilization. *Polym Eng Sci*. 1989;29:782-790.
12. Lee ST. Shear effects on thermoplastic foam nucleation. *Polym Eng Sci*. 1993;33:418-422.
13. Chen L, Wang X, Straff R, Blizard K. Shear stress nucleation in microcellular foaming process. *Polym Eng Sci*. 2002;42:1151-1158.
14. Guo MC, Peng YC. Study of shear nucleation theory in continuous microcellular foam extrusion. *Polym Test*. 2003;22:705-709.
15. Pereira A, McGrath G, Joseph DD. Flow and stress induced cavitation in a journal bearing with axial throughput. *J Tribol*. 2001;123:742-754.
16. Bird RB, Armstrong RC, Hassager O. *Dynamics of Polymeric Liquids: Fluid Mechanics*. Vol. 1, 2nd Edition. New York, NY: Wiley; 1987.
17. Young, FR. *Cavitation*. London: Imperial College Press; 1999.
18. Kell G. Early observations of negative pressures in liquids. *Am J Phys*. 1983;51:1038-1041.
19. Kottke P, Bair S, Winer WO. The measurement of viscosity of liquids under tension. *J Tribol*. 2003;125:260-266.
20. Harvey E, Barnes K, McElroy W, Whitely A, Pease D, Cooper K. Bubble formation in animals. I. Physical factors. *J Cell Comp Physiol*. 1944;25:1-22.
21. Apfel RE. The role of impurities in cavitation-threshold determination. *J Acoust Soc Am*. 1970;48:1179-1186.
22. Crum LA. Nucleation and stabilization of mirobubbles in liquids. *Appl Sci Res*. 1982;38:101-115.
23. Strasberg M. Onset of ultrasonic cavitation in tap water. *J Acoust Soc Am*. 1959;31:163-176.
24. Winterton RHS. Sizes of bubbles produced by dissolved gas coming out of solution on the walls of pipes in flowing systems. *Chem Eng Sci*. 1972;27:1223-1230.
25. Plesset M, Prosperetti A. Bubble dynamics and cavitation. *Ann Rev Fluid Mech*. 1977;9:145-185.
26. Atchley AA, Prosperetti A. The crevice model of bubble nucleation. *J Acoust Soc Am*. 1989;86:1065-1084.
27. Mørch KA. Cavitation nuclei and bubble formation—A dynamic liquid–solid interface problem. *J Fluids Eng*. 2000;122:494-498.
28. Wagner MH. Prediction of primary normal stress difference from shear viscosity data using a single integral constitutive equation. *Rheol Acta*. 1977;16:43-50.
29. Macosko CW. *Rheology: Principals, Measurements and Applications*. New York, NY: VCH; 1994.
30. Gleiβle W. Stresses in polymer melts at the beginning of flow instabilities (melt fracture) in cylindrical capillaries. *Rheol Acta*. 1982;21: 484-487.
31. Tanner RI. *Engineering Rheology*. 2nd Edition. New York, NY: Oxford Univ. Press; 2000.
32. Tanveer S, Vasconcelos GL. Time-evolving bubbles in two-dimensional Stokes flow. *J Fluid Mech*. 1995;301:325-344.
33. Bird RB, Stewart WE, Lightfoot EN. *Transport Phenomena*. 2nd Edition. New York, NY: Wiley; 2002.
34. de Genes PG. Wetting: Statics and dynamics. *Rev Mod Phys*. 1985; 57:827-863.
35. Huh C, Scriven LE. Hydrodynamic model of steady movement of a solid/liquid/fluid contact line. *J Colloid Interface Sci*. 1971;35:85-101.
36. Smith MK. Thermocapillary migration of a two-dimensional liquid droplet on a solid surface. *J Fluid Mech*. 1995;294:209-230.
37. Hoffman RL. A study of the advancing interface. I. Interface shape in liquid– gas systems. *J Colloid Interface Sci*. 1975;50:228-241.
38. Cox RG. The dynamics of the spreading of liquids on a solid surface. Part 1. Viscous flow. *J Fluid Mech*. 1986;168:169-194.
39. Blake TD, Haynes JM. Kinetics of liquid/liquid displacement. *J Colloid Interface Sci*. 1977;30:421-423.
40. Jiang T, Oh S, Slattery JC. Correlation for dynamic contact angle. *J Colloid Interface Sci*. 1979;69:74-77.
41. Pozrikidis C. Interfacial dynamics for Stokes flow. *J Comput Phys*. 2001;169:250-301.
42. Pozrikidis C. Expansion of a compressible gas bubble in Stokes flow. *J Fluid Mech*. 2001;442:171-189.
43. Pozrikidis C. Computation of the pressure inside bubbles and pores in Stokes flow. *J Fluid Mech*. 2003;474:319-337.
44. Dimitrakopoulos P, Higdon JJL. Displacement of fluid droplets from solid surfaces in low-Reynolds-number shear flows. *J Fluid Mech*. 1997;336:351-378.
45. Schleizer A, Bonnecaze R. Displacement of a two-dimensional immiscible droplet adhering to a wall in shear and pressure-driven flows. *J Fluid Mech*. 1999;383:29-54.
46. Stoer J, Bulirsch R. *Introduction to Numerical Analysis*. 2nd Edition. New York, NY: Springer-Verlag; 1992.
47. Power H, Wrobel LC. *Boundary Integral Methods in Fluid Mechanics*. Boston, MA: Computational Mechanics Publications; 1995.
48. Feng J, Basaran O. Shear flow over a translationally symmetric cylindrical bubble pinned over a slot in a plane wall. *J Fluid Mech*. 1994;275:351-378.
49. Rallison JM. The deformation of small viscous drops and bubbles in shear flows. *Ann Rev Fluid Mech*. 1984;16:45-66.
50. de Bruijn RA. Tipstreaming of drops in simple shear flow. *Chem Eng Sci*. 1993;48:277-284.
51. Hirose T, Kamiya Y, Mizoguchi K. Gas transport in poly[bis(trifluoroethoxy)phosphazene]. *J Appl Polym Sci*. 1989;38:809-820.
52. Leal LG. Particle motions in a viscous fluid. *Ann Rev Fluid Mech*. 1980;12:435-476.
53. Uijttewaal WSJ, Nijhof E, Heethaar RM. Droplet migration, deforma-

tion and orientation in the presence of a plane wall: A numerical study compared with analytical theories. *Phys Fluids A*. 1993;5:819-825.
54. Smart JR, Leighton DT. Measurement of the drift of a droplet due to the presence of a plane. *Phys Fluids A*. 1991;3:21-28.
55. Magnaudet J, Takagi S, Legendre D. Drag, deformation and lateral migration of a buoyant drop moving near a wall. *J Fluid Mech*. 2002;476:115-157.
56. Crowdy DG. Compressible bubbles in Stokes flow. *J Fluid Mech*. 2003;476:345-356.
57. Richardson S. Two dimensional bubble in slow viscous flow. *J Fluid Mech*. 1968;33:476-493.
58. Favelukis M, Tadmor Z, Talmon Y. Bubble dissolution in viscous liquids in simple shear flow. *AIChE J*. 1995;41:2637-2641.
59. Duda JL, Vrentas JS. Perturbation solutions of diffusion-controlled moving boundary value problems. *Chem Eng Sci*. 1969;24:461-470.
60. Kontopoulou M, Vlachopoulos J. Bubble dissolution in molten polymers and its role in rotational molding. *Polym Eng Sci*. 2001;39:1189-1198.
61. Epstein PS, Plesset MS. On the stability of gas bubbles in liquid–gas solutions. *J Chem Phys*. 1950;18:1505-1509.
62. Carslaw HS, Jaeger JC. *The Conduction of Heat in Solids*. Oxford, UK: Clarendon Press; 1959.

Appendix

The problem of an expanding or contracting spherical gas bubble in a liquid has been addressed numerous times, starting apparently with Lord Rayleigh, and a thorough review of the literature was performed by Plesset and Prosperetti.[25] Assuming that the bubble is not translating, the resulting flow is irrotational and can be described with a potential function, such that $\partial\phi^*/\partial r^* = u_r^*$. The solution corresponds to that for a point source or sink with time-varying strength $m(t^*)$, and is one dimensional, $\mathbf{u}^* = (u_r^*, 0, 0)$. For unsteady irrotational flow, Bernoulli's equation is

$$\frac{\partial\phi^*}{\partial t^*} + \frac{1}{2}|\mathbf{u}^*|^2 + \frac{p^*}{\rho} - \mathbf{g}\cdot\mathbf{x}^* = c(t^*) \tag{A1}$$

Substituting the velocity and corresponding potential for a point source into Eq. A1 on the bubble surface ($\mathbf{x}^* = R^*$) and as $\mathbf{x}^* \to \infty$, and neglecting body forces, yields

$$\frac{p^*(R^*) - p_\infty^*}{\rho} = \frac{3}{2}\dot{R}^{*2} + R^*\ddot{R}^* \tag{A2}$$

The dynamic boundary condition on the bubble surface relates the pressure in the liquid to the pressure of the gas in the bubble

$$p_B^* = p^*(R^*) - 4\mu\frac{\dot{R}^*}{R^*} + 2\frac{\gamma}{R^*} \tag{A3}$$

By combining Eqs. A2 and A3 we obtain a form of the Rayleigh equation

$$\frac{3}{2}\dot{R}^{*2} + R^*\ddot{R}^* + 4\nu\frac{\dot{R}^*}{R^*} = \frac{p_B^* - p_\infty^* - 2\dfrac{\gamma}{R^*}}{\rho} \tag{A4}$$

The bubble pressure varies as a consequence of an equation of state, which we take to be the ideal gas equation of state

$$p_B^* = c_B^* R_u T \tag{A5}$$

where generally the molar gas concentration in the bubble c_B^* and temperature T are found by solving species and energy conservation equations. We assume that the system will remain isothermal because of the slow rates of dissolution seen for bubbles in our experimental systems. We assume binary Fickian diffusion of a single dissolved gas species in the liquid and, because we expect velocities to be small, we neglect advection

$$\frac{\partial c^*}{\partial t^*} = \frac{D}{r^{*2}}\frac{\partial}{\partial r^*}\left(r^{*2}\frac{\partial c^*}{\partial r^*}\right) \tag{A6}$$

Assuming that far from the bubble the liquid is saturated with gas, the boundary conditions are, from Henry's law

$$c^*(R^*) = Hp_B^* \qquad c^*(r^* \to \infty) = Hp_\infty^* \tag{A7}$$

The solution to the mass conservation problem (Eqs. A6 and A7) is used to find the concentration gradient at the bubble surface, which is incorporated into a statement of species conservation for the bubble

$$\frac{4}{3}\pi\frac{d}{dt^*}(R^{*3}c_B^*) = 4\pi DR^{*2}\left.\frac{\partial c^*}{\partial r^*}\right|_{r^*=R^*} \tag{A8}$$

The system requires initial conditions for completeness. The initial species concentration is taken to be everywhere saturated

$$c^*(t^* = 0) = Hp_\infty^* \tag{A9}$$

The initial bubble size depends on the situation of interest. The resulting system can be solved numerically, using, for instance, a finite-difference method.[59,60] Instead, we make a simplification first reported by Epstein and Plesset.[61] The simplification concerns the gas-diffusion problem. By neglecting the motion of the bubble surface, the concentration gradient at the surface is found to be approximately

$$\left.\frac{\partial c^*}{\partial r^*}\right|_{R^*} \approx -H(p_B^* - p_\infty^*)\left(\frac{1}{R^*} + \frac{1}{\sqrt{\pi D t^*}}\right) \tag{A10}$$

so that Eq. A8 becomes

$$3\dot{R}^* c_B^* + R^*\dot{c}_B^* \approx -3DH(p_B^* - p_\infty^*)\left(\frac{1}{R^*} + \frac{1}{\sqrt{\pi D t^*}}\right) \tag{A11}$$

The equation of state, Eq. A5, and its derivative with respect to time are used to replace c_B and its time derivative in Eq. A11

$$\dot{p}_B^* \approx -3R_u THD\frac{(p_B^* - p_\infty^*)}{R^*}\left(\frac{1}{R^*} + \frac{1}{\sqrt{\pi D t^*}}\right) - 3p_B^*\frac{\dot{R}^*}{R^*} \tag{A12}$$

The model is made nondimensional with the following scales

$$L_s = R_0 \qquad p_s = \frac{\gamma}{R_0} \qquad t_s = \frac{\mu R_0}{\gamma} \tag{A13}$$

so that Eq. A4 becomes

$$\frac{3}{2}\dot{R}^2 + R\ddot{R} + \frac{\mu^2}{\rho\gamma R_0}\left(\frac{4\dot{R}}{R} - p_B + p_\infty + \frac{2}{R}\right) = 0 \tag{A14}$$

where the nondimensional group in front of the parenthesis is the ratio of the capillary number (Ca) to the Reynolds number (Re) and is much greater than 1 for bubble dissolution in a highly viscous liquid. Thus, neglecting the first two (inertial) terms in Eq. A14 and also scaling Eq. A12, we have the simplified dimensionless model of Eq. 38.

Persistence of nuclei in crevices

We next consider the effect of locating the bubble on a solid wall on the rate of dissolution. First we note that if the bubble were a hemisphere on a flat wall with fixed contact angles of $\pi/2$ then the solution to the species conservation problem would be the same as above resulting from symmetry. The flow would no longer be spherically symmetric because of the no-slip boundary condition at the wall. If instead the contact line is pinned on a crevice then the problem loses its spherical symmetry completely, even if the crevice mouth is circular and the bubble surface is assumed to maintain the shape of a spherical cap. We will consider such a case of a crevice with a circular mouth whose radius is equal to the initial bubble radius. The crevice is defined by its volume V_c and the initial bubble radius R_0. The dissolution problem here is clearly quite different from the case of a free bubble. The main difference is explained by the fact that, as gas leaves the bubble and the bubble volume decreases, the mean curvature of the bubble surface κ_m decreases instead of increasing. Thus the pressure in the bubble decreases with time, reducing the driving force for diffusion. The bubble will asymptotically approach a steady solution of zero curvature. Note that this assumes the contact line does not move into the crevice as the contact angle increases.

To retain the simplicity of the solution developed for a free bubble, we revisit that problem and seek to replace terms in that solution with terms from the crevice-stabilized problem. The resulting solution will provide order-of-magnitude estimates. First we consider Eq. A10. The second term in parentheses is essentially the inverse of the penetration depth for one-dimensional diffusion into an infinite medium. We retain it unaltered for the crevice-stabilized bubble solution. The first term in parentheses thus accounts for the multidimensionality of the diffusion. In the case of spherical spreading then this term becomes $1/R$. We seek to include this effect in our nonspherically symmetric problem by approximating the bubble as a shrinking hemisphere. We replace R with an equivalent radius

$$R_{eq} = \frac{A_B}{C_B} \tag{A15}$$

where A_B is the area of the bubble surface and C_B is the arclength of the contact line. Note that for a hemisphere $R_{eq} = R$. Thus we use a generalized version of Eq. A10 to calculate an average molar flux from the bubble

$$\bar{n}''^* \approx HD(p_B^* - p_\infty^*)\left(\frac{1}{R_{eq}^*} + \frac{1}{\sqrt{\pi D t^*}}\right) \tag{A16}$$

Species conservation for the bubble is

$$\frac{d}{dt^*}\left[(V_B^* + V_C^*)\frac{p_B^*}{R_u T}\right] = -HD(p_B^* - p_\infty^*)\left(\frac{1}{R_{eq}^*} + \frac{1}{\sqrt{\pi D t^*}}\right)A_B^* \tag{A17}$$

where V_B^* is the volume of the bubble outside of the crevice and V_C^* is the volume of the crevice. Upon rearrangement and nondimensionalization

$$\frac{dp_B}{dt} = -\Pi_1\frac{(p_B - p_\infty)A_B}{(V_B + V_C)}\left(\frac{C_B}{A_B} + \Pi_2\frac{t^{-1/2}}{\sqrt{\pi}}\right) - \frac{dV_B}{dt}\frac{p_B}{(V_B + V_C)} \tag{A18}$$

For a spherical cap the following formulae are from geometry (made dimensionless)

$$V_B = \frac{\pi h^2}{3}\left(\frac{3}{\kappa_m} - h\right) \qquad A_B = 2\pi\frac{h}{\kappa_m} \qquad C_B = 2\pi$$

$$h = \frac{1}{\kappa_m}\left(1 - \sqrt{1 - \kappa_m^2}\right) \tag{A19}$$

which makes

$$\frac{dV_B}{dt} = -\pi\frac{\kappa_m^2 + 2\sqrt{1 - \kappa_m^2} - 2}{\kappa_m^4\sqrt{1 - \kappa_m^2}}\dot{\kappa}_m \tag{A20}$$

Substituting into Eq. A18, yields, for the case of a pinned contact line, a circular crevice mouth, and spherical cap bubble, a first-order differential equation in time with dependent variables p_B and κ_m that we can write in the form

$$\dot{p}_B = f_1(p_B, \kappa_m, \dot{\kappa}_m, t; \Pi_1, \Pi_2, p_\infty) \tag{A21}$$

For the fluid mechanics portion of the model we start with Eq. A14 and again neglect the inertial terms. We replace $1/R$ in the last term in parentheses with the mean curvature κ_m, and treat the normal viscous stress term in the same manner in which we handled the diffusion problem, using the equivalent radius to capture effects ascribed to changing geometry. This introduces the largest error of all our approximations because, even in the case of a shrinking hemisphere, this will not correctly model the effects of the wall. Nevertheless, we expect that it will provide a reasonable approximation of the contribution of normal viscous stresses. For the case of a pinned contact line, a circular crevice mouth, and spherical cap bubble the resulting equation is

$$\frac{d}{dt}\left(\frac{h}{\kappa_m}\right) = \left(\frac{p_B - p_\infty}{4\kappa_m} - \frac{1}{2}\right)h \tag{A22}$$

Upon substitution of the definition of h from Eq. A19, Eq. A22 can be rearranged as follows

$$\dot{\kappa}_m = f_2(\kappa_m, p_B; p_\infty) \tag{A23}$$

Therefore the problem requires the solution of two, coupled, nonlinear first-order ordinary differential equations. Once again, we limited consideration to initial conditions of a hemispherical bubble in mechanical equilibrium

$$\kappa_m(0) = 1 \qquad p_B(0) = p_\infty + 2 \tag{A24}$$

Two-dimensional bubble

The limiting case of a bubble that is distorted so that it is long in one direction is an infinite cylindrical bubble, which can be used to approximate the case of a bubble where variations in the long direction are small. Thus a polar coordinate system can make sense for modeling a bubble stabilized on a long, narrow, scratchlike crevice. A free cylindrical bubble is not physically realistic but is the starting point for the analysis.

For the case of a two-dimensional (cylindrical) bubble the potential flow solution method cannot be applied in a straightforward manner because the potential does not vanish at infinity; however, the spherical bubble analysis suggests that the effect of the viscous stress will not be important for the experimental liquids and is thus neglected. The dynamic boundary condition for a cylindrical bubble becomes

$$(p_B^* - p_\infty^*) = \frac{\gamma}{R^*} \tag{A25}$$

Because we expect velocities to be small, we again neglect advection so, for the one-dimensional cylindrical system,

$$\frac{\partial c^*}{\partial t^*} = \frac{D}{r^*}\frac{\partial}{\partial r^*}\left(r^*\frac{\partial c^*}{\partial r^*}\right) \tag{A26}$$

In cylindrical coordinates, neglecting the motion of the bubble surface, and applying the same boundary and initial conditions as before (Eqs. A7 and A9) yield the concentration gradient at the surface

$$\left.\frac{\partial c^*}{\partial r^*}\right|_{R^*} \approx -4\frac{H(p_B^* - p_\infty^*)}{\pi^2 R^*}\int_0^\infty \frac{\exp\left(-\frac{Dt^*}{R^{*2}}\tau^2\right)}{\tau[J_0^2(\tau) + Y_0^2(\tau)]}d\tau \tag{A27}$$

where Eq. A27 is found by Laplace transform, J_0 and Y_0 are Bessel's functions, and Eq. A27 must be numerically evaluated.[62]

Species conservation for the bubble requires at the bubble surface

$$\frac{d}{dt^*}(R^{*2}c_B^*) = 2R^*D\left.\frac{\partial c^*}{\partial r^*}\right|_{R^*} \tag{A28}$$

so that Eqs. A27 and A28 are combined to yield

$$2\dot{R}^*Rc_B^* + R^{*2}\dot{c}_B^* = -\frac{8}{\pi^2}DH(p_B^* - p_\infty^*)\int_0^\infty \frac{\exp\left(-\frac{Dt^*}{R^{*2}}\tau^2\right)}{\tau[J_0^2(\tau) + Y_0^2(\tau)]}d\tau \tag{A29}$$

Combining Eq. A29 with the equation of state and its time derivative to eliminate bubble gas concentration terms, and with the dynamic boundary condition and its time derivative to eliminate bubble pressure terms, rearranging, and nondimensionalizing as before,

$$\dot{R} = -\frac{8}{\pi^2}\frac{\Pi_1}{R(2p_\infty R + 1)}\int_0^\infty \frac{\exp\left(-\frac{t}{\Pi_2^2 R^2}\tau^2\right)}{\tau[J_0^2(\tau) + Y_0^2(\tau)]}d\tau \tag{A30}$$

with initial condition

$$R(0) = 1 \tag{A31}$$

Note that the problem depends on the same three parameters as the previous cases.

Following the method used to extend the free spherical bubble to the sphere cap/crevice bubble, we rewrite Eq. A25 as

$$(p_B^* - p_\infty^*) = \gamma\kappa^* \tag{A32}$$

and Eq. A27 as

$$\bar{n}''^* \approx 4\frac{HD(p_B^* - p_\infty^*)}{\pi^2 R_{eq}^*}\int_0^\infty \frac{\exp\left(-\frac{Dt^*}{R_{eq}^{*2}}\tau^2\right)}{\tau[J_0^2(\tau) + Y_0^2(\tau)]}d\tau \tag{A33}$$

where now we define R_{eq} as the average distance from the center of the crevice mouth to the bubble surface, which is expressed nondimensionally in Eq. 44. Note that R_{eq} goes from unity when $\kappa = 1$, to 1/2 as κ approaches zero, just as the sphere cap equivalent radius does.

For the crevice topped with a circular section bubble,

$$\frac{d}{dt^*}[(A_B^* + A_C^*)c_B^*] = -\bar{n}''^*S_B^* \tag{A34}$$

where A_B^* is the cross-sectional area of the bubble outside the crevice, A_C^* is the cross-sectional area of the crevice, and S_B^* is the arclength of the surface of the bubble cross section. Nondimensionalized with R_0 we have

$$\theta = 2\sin^{-1}(\kappa) \qquad A_B = \frac{\theta - \sin\theta}{2\kappa^2} \qquad S_B = \frac{\theta}{\kappa} \tag{A35}$$

and Eq. A34 becomes Eq. 40.

Far-wall effect

The presence of walls increases nuclei persistence in ways other than just providing a crevice. Walls will hinder diffusion, which will allow even free bubbles near the wall to persist for longer times. To get an idea of how much of an effect this will have on bubble life we use the following rough approximation. Consider a crevice-stabilized cylindrical bubble on one of two parallel walls separated by a distance d^*. When the diffusion penetration depth, $\delta = (\pi D t^*)^{1/2}$, has not reached the other wall, the solution is still the solution to the bubble diffusing into a semi-infinite domain, so Eq. 40 applies for times $< t_\delta$, where

$$t_\delta = \frac{\Pi_2^2 (d-h)^2}{\pi} \tag{A36}$$

and h, the distance from the plane of the wall to the furthest point on the bubble, is

$$h = \frac{1 - \sqrt{1-\kappa^2}}{\kappa} \tag{A37}$$

For times sufficiently greater than t_δ the components of the concentration gradients at the bubble surface in the direction perpendicular to the walls will essentially vanish. A conservative approach to including this effect is to say that for $t \gg t_\delta$, the effective arclength for diffusion from the bubble is reduced from S_B to the projection of S_B perpendicular to the walls. This results in replacing S_B in Eq. A34 with $2h$. This approach is conservative because it neglects the effective reduction in cylindrical "spreading" resulting from the presence of the wall. The incorporation of this effect in modeling the dissolution of a cylindrical crevice-stabilized bubble into a bounded domain was accomplished by replacing Eq. 40 with Eq. 44 for $t > 10t_\delta$.

Manuscript received Jun. 22, 2004, and revision received Dec. 8, 2004.